Monte Carlo simulation of the Gross-Neveu model in a fermion loop representation

Diplomarbeit

von

Verena Hermann

aus

Traunstein

durchgeführt am Institut für Theoretische Physik
der Universität Regensburg
und am Institut für Physik, Fachbereich Theoretische Physik
der Karl-Franzens-Universität Graz

unter Anleitung von

Prof. Dr. Klaus Richter und

Prof. Dr. Christof Gattringer

November 2006

Abstract

The Gross-Neveu (GN) model is a 2-dimensional quantum field theory (QFT) with an interaction given by a 4-Fermi term. Already being understood in some detail, it serves as a possibility to explore new strategies for calculating observables or to examine new algorithms.

In this diploma thesis an algorithm for the fermion loop representation of the GN model is developed; on the one hand to confirm the theory, on the other hand to evaluate the pros and cons of the new approach. The work is divided into three main parts:

The first part introduces the GN model on the lattice. The fermion loop representation is derived via rewriting the partition function of a generalized 8-vertex model.

The second part contains the introduction of the new numerical algorithm for fermion loops. The newly developed Monte Carlo loop algorithm faces the challenge of creating and annihilating closed self-avoiding loops with different colors. Ergodicity, boundary conditions and equilibration time are analyzed in detail.

The third part is dedicated to presenting the achieved results. Bulk observables that are rather easy to compute serve as the simplest way to compare the produced data to those obtained from standard methods or analytic results (in the free case). Furthermore, 2-point functions are analyzed, which finally allow conclusions about the mass spectrum. The thesis closes with a critical assessment of the loop approach to the GN model.

Contents

1 Introduction **1**

2 Gross-Neveu-type models in path integral formalism **5**

2.1 The Euclidean path integral 5

2.2 2-point functions and their interpretation 6

2.3 Action for Gross-Neveu-type models 7

2.4 Symmetries 8

3 The Gross-Neveu model on the lattice **11**

3.1 Introduction of the lattice 11

3.2 Grassmann variables 12

3.2.1 Fundamental properties of Grassmann algebras 12

3.2.2 Formulas for Grassmann integrals 13

3.3 The partition function of the Gross-Neveu model 15

4 Fermion loop representation **17**

4.1 Loop representation of the Gross-Neveu model 17

4.2 The generalized 8-vertex model 19

4.2.1 Grassmann representation 20

4.2.2 Hopping expansion 22

4.3 Fermion loop representation 22

5 Monte Carlo methods **25**

5.1 Simple sampling vs. importance sampling 25

5.2 Markov chain 26

5.3 Metropolis algorithm 27

5.4 Error estimation 28

6 Algorithm for fermion loops **29**

6.1 Structure of the computer program 29

6.2 How an update is implemented 30

6.3 Ergodicity 34

6.4 Initial conditions 35

6.5 Equilibration 40

7 Bulk Observables **43**

7.1 Chiral condensate and mass susceptibility 43

7.2 Interaction density and interaction susceptibility 47

7.3 Phase transition / Cross-over 47

8 Finite size effects **51**

8.1 Extrema of the susceptibilities 51

8.2 Comparison of different boundary conditions 53

9 Comparison with standard methods **57**

9.1 The standard approach 57

9.2 Chiral condensate and mass susceptibility 58

9.3 Interaction density 63

10 Scalar 2-point functions **65**

10.1 2-point functions in the loop approach 65

10.2 2-point functions in compare with the standard approach 67

11 Conclusions **71**

11.1 Standard approach versus loop approach 71

11.2 Outlook 73

Appendix **74**

A The doubling problem **75**

B Computing the norm of the hopping matrix $R(\mathbf{n}, \mathbf{m})$ **77**

References **79**

Chapter 1

Introduction

Who wants to have the old **Hitachi SR8000-F1** from the Leibniz-Rechenzentrum? This was the question in an E-mail in June 2006. The Hitachi SR8000-F1 was the flagship high-performance computer at the Leibniz-Rechenzentrum in Munich. It achieved 2.0 TFlops peak performance and had 1376 GByte disk space. On September, 21st, Hitachi SR 8000-F1 was replaced by the new National Supercomputer **HLRB II** (SGI Altix 4700), which has a peak performance of 26.2 TFlops and a total memory size of 17.5 TByte. Moreover, this machine will be upgraded further in 2007.

In practice more disk space means, i.e., for people doing quantum field theory (QFT) on the lattice that larger lattice sizes can be used. This is an advantage as in the physical limit the volume of the system would be infinite. But there exists still another serious problem for the numerical simulation of fermionic systems: The implementation of Pauli statistics. Due to the fermions' antisymmetric wavefunction, terms with opposite sign lead to large cancellations. The consequence is that statistical errors increase exponentially [1] with the volume V of the system. In order to achieve accuracy to a given precision, the computational cost increases exponentially with the volume:

$$\$\$ \propto \mathrm{e}^{cV} , \quad c = \text{const.} \tag{1.1}$$

Even the improved computer performance cannot beat this exponential. Hence, numerical methods to overcome the fermion sign problem would be a tremendous advantage.

C. Gattringer invented an alternative representation - the fermion loop representation for the partition function of the Gross-Neveu (GN) model [2]. The

partition function of this 2-dimensional fermionic model is rewritten as a sum over closed loops with only positive weights. Therefore, simulations on large lattices ($\mathcal{O}(10^4)$ lattice points) are possible, since one is not limited by the sign problem. Additionally, less disk space is needed, and so, even personal computers cope with the task.

In this diploma thesis an algorithm for the fermion loop representation is developed; on the one hand to confirm the theory, on the other hand to evaluate the pros and cons of the alternative approach. The thesis is structured as follows:

Chapter 2 presents the basic formulas for calculating expectation values of observables starting from the action of the system. The action of the GN model is discussed in different formulations and its behavior under symmetry transformations is analyzed. In the one flavor case there exist several equivalent formulations of the interaction, which are summarized. The lattice is introduced in Chapter 3. To understand how the GN model can be simulated on the lattice, it is necessary to present the concept of Grassmann algebras, which provide the correct calculation rules for fermions. Chapter 4 lists the essential steps in the derivation of the fermion loop representation of the GN model. First, one has to apply the hopping expansion to the determinant of the Dirac matrix. Therewith, the partition function can be interpreted as a model of loops. The simulation is still not directly possible at this point, because the loops appear in the exponent. To find the full expansion in terms of loops, the hopping expansion is also applied to a generalized 8-vertex model. Matching the two expanded formulations, one finally arrives at the fermion loop representation, which is now suitable for a Monte Carlo simulation. Monte Carlo simulations are explained in Chapter 5. The Metropolis algorithm used later in the simulation is outlined and the Jackknife method as a possibility for the error estimation is presented. Eventually, Chapter 6 gives the details of the algorithm for fermion loops developed in this work. After explaining the general structure of the program, the more technical aspects are discussed. It is shown how updates can be implemented and in which way the algorithm is ergodic. Different initial conditions are analyzed as well as the equilibration time, which depends on several parameters. A few bulk observables like, e.g., the chiral condensate are discussed in Chapter 7 and signatures of a phase transition / cross-over behavior are investigated. Finite size effects, arising from the extrema of the susceptibilities and from the different types of boundary conditions in the two approaches, are studied in Chapter 8. Chapter 9 contains the comparison between results from the fermion loop representation and those obtained from standard methods or from Fourier transformation, which can be

applied in the free case. In Chapter 10 scalar 2-point functions are presented and their evaluation in the fermion loop representation is discussed. Besides, the analogy to the standard approach is given. Chapter 11 consists of the summary and an outlook. The advantages and disadvantages of the fermion loop representation compared to standard methods are addressed.

Chapter 2

Gross-Neveu-type models in path integral formalism

In this chapter the framework of Euclidean path integrals and the models analyzed in this work are presented. Also their symmetries for various numbers of flavors are discussed.

2.1 The Euclidean path integral

In the path integral formalism vacuum expectation values of observables O in systems characterized by an action S are computed as

$$\langle O \rangle = \frac{1}{Z} \int \mathrm{D}[\psi, \bar{\psi}, \phi] \; e^{-S[\psi,\bar{\psi},\phi]} \; O[\psi, \bar{\psi}, \phi] \; , \tag{2.1}$$

where the integration measure for the fields $\psi, \bar{\psi}$ (fermions) and ϕ (scalar field) is formally defined as

$$\mathrm{D}[\psi, \bar{\psi}, \phi] = \prod_{\mathbf{x}} \mathrm{d}\psi(\mathbf{x}) \mathrm{d}\bar{\psi}(\mathbf{x}) \mathrm{d}\phi(\mathbf{x}) \; . \tag{2.2}$$

The partition function Z is given by

$$Z = \int \mathrm{D}[\psi, \bar{\psi}, \phi] \; e^{-S[\psi,\bar{\psi},\phi]} \; . \tag{2.3}$$

It is the fundamental quantity in statistical mechanics and field theory. All interesting observables can be extracted from Z, when suitable source terms are included. A closed formula for Z (with sources coupled) implies an exact solution of the system.

2.2 2-point functions and their interpretation

The Euclidean correlator $\langle O_2(t)\, O_1(0)\rangle_T$ is called 2-point function and defined as

$$\langle O_2(t)\, O_1(0)\rangle_T = \frac{1}{Z_T}\mathrm{Tr}\left[e^{-(T-t)\hat{H}}\hat{O}_2\, e^{-t\hat{H}}\hat{O}_1\right] . \tag{2.4}$$

The right-hand side can be rewritten as the path integral expression (2.1) (see, e.g., [3, 4]). $\hat{O}_1$ and $\hat{O}_2$ may be arbitrary operators and $\hat{H}$ denotes the Hamiltonian. Its eigenvalues are the energies of the system. The partition function Z_T is given by

$$Z_T = \mathrm{Tr}\left[e^{-T\hat{H}}\right] . \tag{2.5}$$

T and t are Euclidean time variables. T is only formally included and will eventually be taken to infinity, whereas t remains finite. The form (2.4) is particularly convenient to derive the formula necessary for interpreting 2-point functions.

In order to evaluate Eqs. (2.4) and (2.5) one inserts the unit matrix $\mathbb{1} = \sum_n |n\rangle\langle n|$, represented as a spectral sum of the eigenstates $|n\rangle$ of $\hat{H}$. The same set of states is used to compute the trace. One obtains

$$\langle O_2(t)\, O_1(0)\rangle_T = \frac{1}{Z_T}\sum_{n,m}\langle m|\hat{O}_2|n\rangle\langle n|\hat{O}_1|m\rangle\, e^{-(T-t)E_m}e^{-tE_n} . \tag{2.6}$$

The eigenvalues E_n are ordered according to

$$E_0 \le E_1 \le E_2 \le \dots . \tag{2.7}$$

The factor e^{-TE_0}, corresponding to the vacuum energy E_0, cancels in Eq. (2.6) and one finds

$$\langle O_2(t)\, O_1(0)\rangle_T = \frac{\sum_{n,m}\langle m|\hat{O}_2|n\rangle\langle n|\hat{O}_1|m\rangle\, e^{-(T-t)E_m}e^{-tE_n}}{1+e^{-TE_1}+e^{-TE_2}+\dots} , \tag{2.8}$$

with E_n now denoting the energy differences $(E_n - E_0)$ with respect to the (unknown) vacuum energy E_0.

In the limit $T \to \infty$, there remain only those terms with $m = 0$ and the 2-point function reduces to

$$\lim_{T\to\infty}\frac{1}{Z_T}\mathrm{Tr}\left[e^{-(T-t)\hat{H}}\hat{O}_2\, e^{-t\hat{H}}\hat{O}_1\right] = \sum_n \left\langle 0|\hat{O}_2|n\right\rangle \left\langle n|\hat{O}_1|0\right\rangle e^{-tE_n} . \tag{2.9}$$

Thus, one concludes that if O is replaced by a product $O = O_2(t)O_1(0)$ in Eq. (2.1), the energies E_n can be computed from the exponential decay of the 2-point function (2.9).

2.3 Action for Gross-Neveu-type models

In general, the action S is an integral over Euclidean space and time:

$$S[\psi, \bar{\psi}, \phi] = \int \mathrm{d}^2x \; L[\psi, \bar{\psi}, \phi] \; . \tag{2.10}$$

Using a scalar auxiliary field $\phi(\mathbf{x})$ the action density L for the GN model is given by

$$L = \sum_{f=1}^{N_f} \bar{\psi}^{(f)}(\mathbf{x}) \left[\gamma_\mu \partial_\mu + m + \phi(\mathbf{x})\right] \psi^{(f)}(\mathbf{x}) + \frac{1}{2g}\phi^2(\mathbf{x}) \; , \tag{2.11}$$

where m is the mass parameter and g the coupling constant. Here, the fermion fields $\bar{\psi}$ and ψ can explicitly be written as

$$\bar{\psi} = \left(\bar{\psi}_1(\mathbf{x}), \bar{\psi}_2(\mathbf{x})\right) \; , \qquad \psi = \left(\psi_1(\mathbf{x}), \psi_2(\mathbf{x})\right)^{\mathrm{T}} \; . \tag{2.12}$$

$\mathbf{x}$ is a 2-dimensional vector composed of one component for space and one for (Euclidean) time. The superscript (f) labels the N_f different flavors of equal mass. The index μ stands for the two directions in spacetime and the γ_μ are the Pauli matrices

$$\gamma_1 = \begin{pmatrix} 0 & 1 \\ 1 & 0 \end{pmatrix} \; , \qquad \gamma_2 = \begin{pmatrix} 0 & -i \\ i & 0 \end{pmatrix} \; . \tag{2.13}$$

In this formulation the action of the GN model can be divided into two parts, namely the fermionic and the scalar one:

$$\begin{aligned} S[\psi, \bar{\psi}, \phi] &= S_F[\psi, \bar{\psi}, \phi] + S_S[\phi] \; , \\ S_F[\psi, \bar{\psi}, \phi] &= \sum_{f=1}^{N_f} \int \mathrm{d}^2x \; \bar{\psi}^{(f)}(\mathbf{x}) \left[\gamma_\mu \partial_\mu + m + \phi(\mathbf{x})\right] \psi^{(f)}(\mathbf{x}) \; , \\ S_S[\phi] &= \frac{1}{2g} \int \mathrm{d}^2x \; \phi^2(\mathbf{x}) \; . \end{aligned} \tag{2.14}$$

An equivalent formulation for the action, as it is introduced similarly by D. Gross and A. Neveu in [2], follows after the integration over $\phi(\mathbf{x})$ in Eq. (2.1) (*Hubbard-Stratonovich transformation* [5, 6]):

$$\begin{aligned} S_{eff}[\psi, \bar{\psi}] = \int \mathrm{d}^2x \; \Bigg[& \sum_{f=1}^{N_f} \bar{\psi}^{(f)}(\mathbf{x}) \left[\gamma_\mu \partial_\mu + m\right] \psi^{(f)}(\mathbf{x}) \\ & -\frac{g}{2} \left(\sum_{f=1}^{N_f} \bar{\psi}^{(f)}(\mathbf{x}) \psi^{(f)}(\mathbf{x}) \right)^2 \Bigg] \; . \end{aligned} \tag{2.15}$$

Therewith, the model consists of a kinetic part, the mass term and the 4-Fermi term for the interaction. The GN model is asymptotically free, renormalizable (in two dimensions), large-N_f expandable and has dynamical mass generation. Hence, it is an interesting model for 4-dimensional quantum chromodynamics.

2.4 Symmetries

In this section symmetry properties of the above model are discussed.

The Z_2-symmetry is defined by the transformation

$$\begin{aligned} \psi^{(f)}(\mathbf{x}) &\longmapsto \psi^{(f)}(\mathbf{x})' = \gamma_5 \psi^{(f)}(\mathbf{x}) \ , \\ \bar{\psi}^{(f)}(\mathbf{x}) &\longmapsto \bar{\psi}^{(f)}(\mathbf{x})' = -\bar{\psi}^{(f)}(\mathbf{x})\gamma_5 \ . \end{aligned} \tag{2.16}$$

with

$$\gamma_5 = \begin{pmatrix} 1 & 0 \\ 0 & -1 \end{pmatrix} \ . \tag{2.17}$$

The kinetic term ($m = 0$) transforms like

$$\bar{\psi}^{(f)}(\mathbf{x})\gamma_\mu \partial_\mu \psi^{(f)}(\mathbf{x}) \longmapsto -\bar{\psi}^{(f)}(\mathbf{x})\gamma_5\gamma_\mu\partial_\mu\gamma_5\psi^{(f)}(\mathbf{x}) = \bar{\psi}^{(f)}(\mathbf{x})\gamma_\mu\partial_\mu\psi^{(f)}(\mathbf{x}) \ , \tag{2.18}$$

where $\gamma_5^2 = \mathbb{1}$ and the anti-commutation relation $\{\gamma_5, \gamma_\mu\} = 0$ were used. The term $\bar{\psi}^{(f)}(\mathbf{x})\psi^{(f)}(\mathbf{x})$, however, acquires an extra minus sign:

$$\bar{\psi}^{(f)}(\mathbf{x})\psi^{(f)}(\mathbf{x}) \longmapsto -\bar{\psi}^{(f)}(\mathbf{x})\psi^{(f)}(\mathbf{x}) \ . \tag{2.19}$$

This term appears twice in Eq. (2.15), in the mass term and in the 4-Fermi interaction. For the mass term the minus sign is manifest and thus, this term is not invariant. In the 4-Fermi interaction the term $\bar{\psi}^{(f)}(\mathbf{x})\psi^{(f)}(\mathbf{x})$ is squared and no overall minus sign remains. Consequently, the action (2.15) is invariant under (2.16) for $m = 0$. (2.16) is a discrete symmetry and thus can be broken spontaneously also in 2 dimensions.

The transformation (2.16) is a special case of the continuous chiral symmetry

$$\begin{aligned} \psi^{(f)}(\mathbf{x}) &\longmapsto \psi^{(f)}(\mathbf{x})' = e^{\mathrm{i}\theta\gamma_5} \psi^{(f)}(\mathbf{x}) \ , \\ \bar{\psi}^{(f)}(\mathbf{x}) &\longmapsto \bar{\psi}^{(f)}(\mathbf{x})' = \bar{\psi}^{(f)}(\mathbf{x}) e^{\mathrm{i}\theta\gamma_5} \ , \end{aligned} \tag{2.20}$$

where θ is a real parameter. (2.20) is equivalent to the transformation (2.16) for $\theta = \frac{\pi}{2}$. Under the continuous transformation (2.20) the kinetic term still remains invariant and the mass term breaks the symmetry. Concerning the interaction term one has to distinguish between two cases, namely only one flavor or more than one.

For several flavors the massless model would only be invariant under (2.20), if the interaction term was generalized to

$$\left(\sum_{f=1}^{N_f} \bar{\psi}^{(f)}(\mathbf{x})\psi^{(f)}(\mathbf{x})\right)^2 - \left(\sum_{f=1}^{N_f} \bar{\psi}^{(f)}(\mathbf{x})\gamma_5\psi^{(f)}(\mathbf{x})\right)^2 , \tag{2.21}$$

as in the Nambu-Jona-Lasinio model [7, 8].

For $N_f = 1$, already the simpler interaction term, as used in Eq. (2.15), is invariant. Writing the transformation as (2.20) one finds

$$\begin{aligned}
\left[\bar{\psi}(\mathbf{x})\psi(\mathbf{x})\right]^2 \;&\longmapsto\; \left[\bar{\psi}(\mathbf{x})\left(\cos(2\theta) + \mathrm{i}\gamma_5\sin(2\theta)\right)\psi(\mathbf{x})\right]^2 \\
&= \left[\bar{\psi}(\mathbf{x})\psi(\mathbf{x})\right]^2\cos^2(2\theta) - \left[\bar{\psi}(\mathbf{x})\gamma_5\psi(\mathbf{x})\right]^2\sin^2(2\theta) \\
&\quad + 2\mathrm{i}\cos(2\theta)\sin(2\theta)\bar{\psi}(\mathbf{x})\psi(\mathbf{x})\bar{\psi}(\mathbf{x})\gamma_5\psi(\mathbf{x}) \\
&= \left[\bar{\psi}(\mathbf{x})\psi(\mathbf{x})\right]^2 ,
\end{aligned} \tag{2.22}$$

where the identity

$$\begin{aligned}
\left[\bar{\psi}(\mathbf{x})\psi(\mathbf{x})\right]^2 &= \left[\bar{\psi}_1(\mathbf{x})\psi_1(\mathbf{x}) + \bar{\psi}_2(\mathbf{x})\psi_2(\mathbf{x})\right]^2 \\
&= 2\,\bar{\psi}_1(\mathbf{x})\psi_1(\mathbf{x})\bar{\psi}_2(\mathbf{x})\psi_2(\mathbf{x}) \\
&= -\left[\bar{\psi}_1(\mathbf{x})\psi_1(\mathbf{x}) - \bar{\psi}_2(\mathbf{x})\psi_2(\mathbf{x})\right]^2 \\
&= -\left[\bar{\psi}(\mathbf{x})\gamma_5\psi(\mathbf{x})\right]^2 ,
\end{aligned} \tag{2.23}$$

and the nilpotency of the fermion fields, i.e., $\psi_i^2 = \bar{\psi}_i^2 = 0$ were used (see also Sec. 3.2). For $N_f = 1$, there exists even a third form of the interaction term,

$$\begin{aligned}
&-\frac{1}{2}\left[\sum_{\mu=1}^{2}\bar{\psi}(\mathbf{x})\gamma_\mu\psi(\mathbf{x})\right]^2 \\
&\quad = -\frac{1}{2}\left[\left(\bar{\psi}_1(\mathbf{x})\psi_2(\mathbf{x}) + \bar{\psi}_2(\mathbf{x})\psi_1(\mathbf{x})\right)^2 + \left(-\mathrm{i}\bar{\psi}_1(\mathbf{x})\psi_2(\mathbf{x}) + \mathrm{i}\bar{\psi}_2(\mathbf{x})\psi_1(\mathbf{x})\right)^2\right] \\
&\quad = -\bar{\psi}_1(\mathbf{x})\psi_2(\mathbf{x})\bar{\psi}_2(\mathbf{x})\psi_1(\mathbf{x}) - \bar{\psi}_1(\mathbf{x})\psi_2(\mathbf{x})\bar{\psi}_2(\mathbf{x})\psi_1(\mathbf{x}) \\
&\quad = 2\,\bar{\psi}_1(\mathbf{x})\psi_1(\mathbf{x})\bar{\psi}_2(\mathbf{x})\psi_2(\mathbf{x}) ,
\end{aligned} \tag{2.24}$$

which is the form known from the Thirring model [9].

To summarize, the 1-flavor case provides three equivalent forms of the interaction term

$$\left[\bar{\psi}(\mathbf{x})\psi(\mathbf{x})\right]^2 = -\left[\bar{\psi}(\mathbf{x})\gamma_5\psi(\mathbf{x})\right]^2 = -\frac{1}{2}\left[\bar{\psi}(\mathbf{x})\gamma_\mu\psi(\mathbf{x})\right]^2 \ , \tag{2.25}$$

and the massless model is invariant under the continuous transformation (2.20). In this work, only the 1-flavor model will be considered, with and without mass. Since the 1-flavor model has the continuous symmetry (2.20) (at $m = 0$), one does not expect to find phase transitions from spontaneous symmetry breaking but only cross-over type behavior in general. This expectation will be investigated by the numerical analysis presented below.

Chapter 3

The Gross-Neveu model on the lattice

As it stands, the path integral formulated in Eqs. (2.1)-(2.3) is only formally defined. For a rigorous definition a cutoff has to be introduced.

Lattice QFT is a mathematically well defined formulation at the nonperturbative level with a momentum cutoff proportional to the inverse lattice spacing and in this way it provides a possible regularization. Another advantage of Lattice QFT is the possibility to obtain quantitative results by numerical simulations without being forced to use effective theories or perturbative expansion (see, e.g., [10, 11, 12]).

3.1 Introduction of the lattice

When introducing the lattice, the vector $\mathbf{x} \in \mathbb{R}^2$ is replaced by

$$\mathbf{x} \longmapsto a\,\mathbf{n}, \qquad \mathbf{n} \in \Lambda \ , \ |\Lambda| = L_1 \times L_2 \ , \tag{3.1}$$

with Λ being a two-dimensional lattice consisting of $L_1 \times L_2$ sites $\mathbf{n}$,

$$\Lambda = \{\mathbf{n} = (n_1, n_2) \mid n_\mu = 1, 2, \ldots, L_\mu \ ; \ \mu = 1, 2\} \ . \tag{3.2}$$

L_1 and L_2 denote the number of sites in space and time direction and a is the lattice spacing. Eventually, the continuum limit $a \to 0$ will be considered. For

notational convenience a is set equal to 1, whenever it appears in the arguments of $\psi, \bar{\psi}$ or ϕ in the following. The next step is to discretize the derivative ∂_μ

$$\partial_\mu \longmapsto \frac{\delta_{\mathbf{n},\mathbf{n}+\hat{\mu}} - \delta_{\mathbf{n},\mathbf{n}-\hat{\mu}}}{2a} \ , \tag{3.3}$$

where $\hat{\mu}$ denotes the unit vector in direction of μ. Obviously, for $a \to 0$ the right-hand side approaches ∂_μ.

Now the general formulas for the path integral introduced in Sec. 2.1 can be rewritten in lattice formulation. Again, expectation values are given by

$$\langle O \rangle = \frac{1}{Z} \int \mathrm{D}[\psi, \bar{\psi}, \phi] \ e^{-S[\psi,\bar{\psi},\phi]} \ O[\psi, \bar{\psi}, \phi] \ , \tag{3.4}$$

with

$$Z = \int \mathrm{D}[\psi, \bar{\psi}, \phi] \ e^{-S[\psi,\bar{\psi},\phi]} \ . \tag{3.5}$$

The integration measure is now well defined as the product over all lattice sites

$$\mathrm{D}[\psi, \bar{\psi}, \phi] = \prod_{\mathbf{n}} \mathrm{d}\psi(\mathbf{n}) \mathrm{d}\bar{\psi}(\mathbf{n}) \mathrm{d}\phi(\mathbf{n}) \ . \tag{3.6}$$

3.2 Grassmann variables

Due to the Pauli principle fermions have anti-symmetric n-point functions. In the path integral formalism this is implemented by using so-called Grassmann variables. Here, the basic definitions and the formulas needed later are collected (for a more detailed discussion see [3, 13]).

3.2.1 Fundamental properties of Grassmann algebras

Grassmann variables are anti-commuting numbers $\eta_i, i = 1, \ldots, N$, obeying

$$\eta_i \eta_j = -\eta_j \eta_i \ , \tag{3.7}$$

for any i, j. This equation implies nilpotency ($\eta_i^2 = 0$), which causes the termination of the power series for any function of the η_i after a finite number of terms. All elements of the resulting Grassmann algebra can be expressed as a polynomial

$$A = a + \sum_i a_i \eta_i + \sum_{i<j} a_{ij} \eta_i \eta_j + \sum_{i<j<k} a_{ijk} \eta_i \eta_j \eta_k + \cdots + a_{12\ldots N} \eta_1 \eta_2 \ldots \eta_N \ , \tag{3.8}$$

where the $a, a_i, a_{ij}, \ldots, a_{12\ldots N}$ denote complex coefficients. Based on Eqs. (3.7) and (3.8), one can construct integrals over Grassmann variables characterized by the formulas

$$\int \mathrm{d}\eta_i \; 1 = 0 \; , \quad \int \mathrm{d}\eta_i \; \eta_i = 1 \; , \quad \mathrm{d}\eta_i \mathrm{d}\eta_j = -\mathrm{d}\eta_j \mathrm{d}\eta_i \; . \tag{3.9}$$

Under a linear transformation

$$\eta_i' = \sum_{j=1}^{N} M_{ij} \eta_j \; , \tag{3.10}$$

the integration measure transforms as

$$\int \mathrm{d}^N \eta \; \eta_1 \eta_2 \ldots \eta_N = \det[M] \int \mathrm{d}^N \eta' \; \eta_1 \eta_2 \ldots \eta_N \; . \tag{3.11}$$

For derivatives with respect to Grassmann variables one finds

$$\begin{aligned} \partial_{\eta_i} 1 = 0 \; , \qquad & \partial_{\eta_i} \eta_i = 1 \; , \\ \left\{ \partial_{\eta_i} \; , \; \partial_{\eta_j} \right\} = 0 \; , \qquad & \{ \partial_{\eta_i} \; , \eta_j \} = 0 \; (\text{for } i \neq j) \; , \end{aligned} \tag{3.12}$$

where the curly brackets denote the anti-commutators and $\partial_{\eta_i} = \frac{\partial}{\partial \eta_i}$.

3.2.2 Formulas for Grassmann integrals

In this section Gaussian integrals with Grassmann variables, giving rise to the so-called *Matthews-Salam formula* and *Wick's theorem*, are discussed.

Supposed, the partition function Z is given by

$$Z = \int \mathrm{d}\eta_N \; \mathrm{d}\bar{\eta}_N \ldots \mathrm{d}\eta_1 \mathrm{d}\bar{\eta}_1 \exp \left(\sum_{i,j=1}^{N} \bar{\eta}_i M_{ij} \eta_j \right) \; . \tag{3.13}$$

The integration runs over $2N$ Grassmann variables $\eta_1, \ldots, \eta_N, \bar{\eta}_1, \ldots, \bar{\eta}_N$. M is a $N \times N$ matrix and later will be chosen as the Dirac operator for the GN model on the lattice introduced in Eq. (3.22) below. Applying the transformation (3.10)

to the Gaussian integral (3.13) and using Eq. (3.11), the partition function reads

$$\begin{aligned} Z &= \det[M] \int \left(\prod_{i=1}^{N} \mathrm{d}\eta_i' \mathrm{d}\bar{\eta}_i \right) \exp\left(\sum_{j=1}^{N} \bar{\eta}_j \eta_j' \right) \\ &= \det[M] \prod_{i=1}^{N} \left(\int \mathrm{d}\eta_i' \mathrm{d}\bar{\eta}_i \exp(\bar{\eta}_i \eta_i') \right) \\ &= \det[M] \left(\prod_{i=1}^{N} \int \mathrm{d}\eta_i' \mathrm{d}\bar{\eta}_i (1 + \bar{\eta}_i \eta_i') \right) = \det[M] \ . \end{aligned} \tag{3.14}$$

Turning the sum in the exponent into a product and interchanging the integral with the product is admissible because pairs of Grassmann variables commute with each other. The power series of the exponential function terminates after the second term since Grassmann variables are nilpotent. Following the rules for the integration of Grassmann variables, it turns out that the remaining integral reduces to a factor 1. This result of the Matthews-Salam formula is the reason that the fermionic partition function often is referred to as *fermion determinant*.

The integral for the partition function Eq. (3.13) can be generalized by the *generating functional for fermions*, which is given by

$$\begin{aligned} W[\theta, \bar{\theta}] &= \int \mathrm{d}\eta_N \mathrm{d}\bar{\eta}_N \ldots \mathrm{d}\eta_1 \mathrm{d}\bar{\eta}_1 \exp\left(\sum_{i,j=1}^{N} \bar{\eta}_i M_{ij} \, \eta_j + \sum_{i=1}^{N} \bar{\theta}_i \eta_i + \sum_{i=1}^{N} \bar{\eta}_i \theta_i \right) \\ &= \det[M] \exp\left(- \sum_{n,m=1}^{N} \bar{\theta}_n (M^{-1})_{nm} \, \theta_m \right) \ , \end{aligned} \tag{3.15}$$

where the Grassmann variables θ and $\bar{\theta}$ serve as source terms for further calculations. The second line of Eq. (3.15) results from the following procedure: One rewrites the exponent as

$$\left(\bar{\eta}_i + \bar{\theta}_j (M^{-1})_{ji} \right) M_{ik} \left(\eta_k + (M^{-1})_{kl} \, \theta_l \right) - \bar{\theta}_n (M^{-1})_{nm} \, \theta_m \ , \tag{3.16}$$

and performs a transformation of variables

$$\begin{aligned} \bar{\eta}_i &\longmapsto \bar{\eta}_i' = \bar{\eta}_i + \bar{\theta}_j (M^{-1})_{ji} \ , \\ \eta_k &\longmapsto \eta_k' = \eta_k + (M^{-1})_{kl} \, \theta_l \ . \end{aligned} \tag{3.17}$$

Since the integration measure is invariant (see Eq. (3.11)), this transformation

leads to:

$$\begin{aligned} W[\theta,\bar{\theta}] &= \exp\left(-\sum_{n,m=1}^{N}\bar{\theta}_n(M^{-1})_{nm}\,\theta_m\right)\int\left(\prod_{i=1}^{N}\mathrm{d}\eta_i'\mathrm{d}\bar{\eta}_i'\right)\exp\left(\sum_{i,j=1}^{N}\bar{\eta}_i' M_{ij}\,\eta_j'\right) \\ &= \det[M]\exp\left(-\sum_{n,m=1}^{N}\bar{\theta}_n(M^{-1})_{nm}\,\theta_m\right)\,, \end{aligned} \tag{3.18}$$

where Eq. (3.14) was used. Taking $W[\theta,\bar{\theta}]$ as it is given in the first line of Eq. (3.15), deriving it with respect to the source terms, setting the source terms equal to zero afterwards and dividing the whole term by Z, there results

$$\begin{aligned} &\frac{1}{Z}\frac{\partial}{\partial\theta_{j_1}}\frac{\partial}{\partial\bar{\theta}_{i_1}}\cdots\frac{\partial}{\partial\theta_{j_n}}\frac{\partial}{\partial\bar{\theta}_{i_n}}W[\theta,\bar{\theta}]\Big|_{\theta,\bar{\theta}=0} \\ &= \frac{1}{Z}\int\sum_{k=1}^{N}\mathrm{d}\eta_k'\mathrm{d}\bar{\eta}_k'\,\eta_{i_1}\bar{\eta}_{j_1}\ldots\eta_{i_n}\bar{\eta}_{j_n}\exp\left(\sum_{l,m=1}^{N}\bar{\eta}_l M_{lm}\eta_m\right)\,, \end{aligned} \tag{3.19}$$

which is a common expression for so-called *n-point functions* (compare Secs. 2.1 and 2.2). Thus, n-point functions can also be written as

$$\langle\eta_{i_1}\bar{\eta}_{j_1}\ldots\eta_{i_n}\bar{\eta}_{j_n}\rangle = (-1)^n\sum_{P(1,2,\ldots,n)}\mathrm{sign}(P)\,(M^{-1})_{i_1 j_{P_1}}(M^{-1})_{i_2 j_{P_2}}\ldots(M^{-1})_{i_n j_{P_n}}, \tag{3.20}$$

where the same steps as before were applied to the second line of Eq. (3.15). The sum runs over all permutations P. This is the Wick's theorem [14], which will be needed in Chap. 9 for computing observables with the standard approach.

3.3 The partition function of the Gross-Neveu model

As in the continuum, the action of the GN model can be divided into a scalar and a fermionic part also on the lattice (here, $N_f = 1$):

$$\begin{aligned} S_S[\phi] &= \frac{1}{2g}\sum_{\mathbf{n}\in\Lambda}\phi^2(\mathbf{n})\,, \\ S_F[\psi,\bar{\psi},\phi] &= \sum_{\mathbf{n},\mathbf{m}\in\Lambda}\bar{\psi}(\mathbf{n})M^{[\phi]}(\mathbf{n},\mathbf{m})\psi(\mathbf{m})\,. \end{aligned} \tag{3.21}$$

The Dirac matrix M reads

$$M^{[\phi]}(\mathbf{n},\mathbf{m}) = [2 + m + \phi(\mathbf{n})]\,\delta_{\mathbf{n},\mathbf{m}} - \sum_{\mu=\pm1}^{\pm2} \Gamma_\mu \delta_{\mathbf{n}+\hat{\mu},\mathbf{m}} \ , \tag{3.22}$$

and the matrices Γ_μ are given by

$$\Gamma_{\pm\mu} = \frac{1}{2}\left(\mathbb{1} \mp \gamma_\mu\right) \ . \tag{3.23}$$

A closer look at the Dirac matrix M shows that the naive expression (3.3) for the derivative has been modified by adding 2 to the first term in M and replacing the matrices γ_μ of the second term by the matrices Γ_μ. The reason for this is the so-called *fermion doubling problem*. It is a consequence of the periodic momentum space and may be overcome by adding the extra terms (see App. A). The resulting formulation is referred to as *Wilson fermions*.

The partition function of the GN model on the lattice is given by

$$Z_{GN} = \int \prod_{\mathbf{n}} \frac{\mathrm{d}\phi(\mathbf{n})}{\sqrt{2\pi g}} \int \prod_{\mathbf{n}} \mathrm{d}\psi(\mathbf{n})\mathrm{d}\bar{\psi}(\mathbf{n})\ e^{-\sum_{\mathbf{n},\mathbf{m}\in\Lambda} \bar{\psi}(\mathbf{n}) M^{[\phi]}(\mathbf{n},\mathbf{m})\psi(\mathbf{m})} e^{-\frac{1}{2g}\sum_{\mathbf{n}}\phi^2(\mathbf{n})} \ , \tag{3.24}$$

where the measure $\mathrm{d}\phi(\mathbf{n})$ now is normalized to 1.

As shown in Sec. 3.2.2, according to the Matthews-Salam formula (3.14) the Gaussian integral for fermions is simply $\det[M]$ and one obtains

$$Z_{GN} = \int \prod_{\mathbf{n}} \frac{\mathrm{d}\phi(\mathbf{n})}{\sqrt{2\pi g}} \det[M^{[\phi]}] e^{-\frac{1}{2g}\sum_{\mathbf{n}}\phi^2(\mathbf{n})} \ . \tag{3.25}$$

So, for the evaluation of the partition function, the determinant of M has to be computed. This is the proceeding in the standard approach.

Again, the action can be rewritten into a purely fermionic one by integrating out the scalar field in Eq. (3.24). One finds:

$$S_{eff}[\psi,\bar{\psi}] = \sum_{\mathbf{n},\mathbf{m}} \psi(\mathbf{n}) M^{[\phi=0]}(\mathbf{n},\mathbf{m})\bar{\psi}(\mathbf{m}) - \frac{g}{2}\sum_{\mathbf{n}} \left(\bar{\psi}(\mathbf{n})\psi(\mathbf{n})\right)^2 \ . \tag{3.26}$$

As in the continuum, the 4-Fermi term can be expressed in the 3 different forms listed in Eq. (2.25).

Chapter 4

Fermion loop representation

In this chapter the partition function of the GN model is rewritten as a model of loops. The necessary steps are the hopping expansion of the GN model on the lattice and the identification of a loop model with an identical hopping expansion. The presentation follows [15, 16, 17].

4.1 Loop representation of the Gross-Neveu model

In the following a loop representation of the GN model will be derived by performing the so-called *hopping expansion*. For this purpose, one defines

$$h(\mathbf{n}) = 2 + m + \phi(\mathbf{n}) \ , \tag{4.1}$$

$$R(\mathbf{n},\mathbf{m}) = \frac{1}{h(\mathbf{n})} \sum_{\mu=\pm 1}^{\pm 2} \Gamma_\mu \ \delta_{\mathbf{n}+\hat{\mu},\mathbf{m}} \ , \tag{4.2}$$

and writes the matrix M as

$$M^{[\phi]}(\mathbf{n},\mathbf{m}) = h(\mathbf{n}) \left[\mathbb{1} \ \delta_{\mathbf{n},\mathbf{m}} - R(\mathbf{n},\mathbf{m})\right] \ . \tag{4.3}$$

$\mathbb{1} = \delta_{\alpha,\beta}$ is the unit matrix in Dirac space. In the so-called *hopping matrix* R all nearest neighbor terms are collected. The fermion determinant becomes

$$\begin{aligned} \det\left[M^{[\phi]}\right] &= \left(\prod_{\mathbf{n}} h^2(\mathbf{n})\right) \det\left[\mathbb{1} - R\right] \\ &= \left(\prod_{\mathbf{n}} h^2(\mathbf{n})\right) \exp\Big(\mathrm{Tr}\big[\ln(\mathbb{1} - R)\big]\Big) \\ &= \left(\prod_{\mathbf{n}} h^2(\mathbf{n})\right) \exp\left(-\sum_{k=1}^{\infty} \frac{1}{k} \mathrm{Tr}\left[R^k\right]\right) . \end{aligned} \tag{4.4}$$

A well known formula for determinants was used in the second step and in the last step the logarithm was expanded in a power series, which converges for $\|R\| \leq 1$. This condition is satisfied if $|h(\mathbf{n})| > 2$, because $h \cdot R$ is bounded by 2 (see App. (B)). It has to be remarked that the condition $|h(\mathbf{n})| > 2$ can be lifted later and the expansion holds for arbitrary $\phi(\mathbf{n})$ and m.

The k-th power of R can be written out as

$$R^k(\mathbf{n}, \mathbf{m}) = \sum_{\mathbf{l}_1, \mathbf{l}_2, \ldots, \mathbf{l}_{k-1}} R(\mathbf{n}, \mathbf{l}_1) R(\mathbf{l}_1, \mathbf{l}_2) \ldots R(\mathbf{l}_{k-1}, \mathbf{m}) \ . \tag{4.5}$$

Due to the Kronecker deltas $\delta_{\mathbf{l}_i + \hat{\mu}, \mathbf{l}_j}$ in $R(\mathbf{l}_i, \mathbf{l}_j)$ each factor in Eq. (4.5) combines two neighboring sites. This fact allows to interpret $\mathrm{Tr}\left[R^k\right]$ as a sum over closed loops of length k. Since closed loops consist of an even number of steps, k must be even for nonvanishing $\mathrm{Tr}\left[R^k\right]$. Along the loops, factors of $1/h(\mathbf{n})$ are collected as well as the matrices Γ_μ for the directions of the links in the loops. Thus, (using Eq. (4.2)) one finds

$$\mathrm{Tr}\left[R^{2k}\right] = \sum_{\mathbf{n} \in \Lambda} \sum_{L \in \mathcal{L}_{\mathbf{n}}^{(2k)}} \prod_{\mathbf{m} \in P(L)} \frac{1}{h(\mathbf{m})} \ \mathrm{Tr}\Big[\prod_{\mu \in L} \Gamma_\mu\Big] \ . \tag{4.6}$$

$\mathcal{L}_{\mathbf{n}}^{(2k)}$ is the set of all possible loops of length $2k$ and starting point $\mathbf{n}$. $P(L)$ denotes the set of sites visited by the loop L. Note that $\mathbf{n}$ is included in $P(L)$ as well and sites have to be counted according to the multiplicity of being visited by the loop. An important property of the loops is the fact that they may not contain 180° turns (no back-tracking). This follows from the second of the projector properties of the Γ_μ:

$$\Gamma_\mu^2 = \Gamma_\mu \ , \ \Gamma_\mu \cdot \Gamma_{-\mu} = \frac{1}{2}(1 - \gamma_\mu) \cdot \frac{1}{2}(1 + \gamma_\mu) = 0 \ . \tag{4.7}$$

There remains to compute the trace over all matrices Γ_μ contained in the loops. Exploring the projector properties (4.7) and the algebra of the Pauli matrices, one finds [18, 19, 20]

$$\mathrm{Tr}\Big[\prod_{\mu\in L}\Gamma_\mu\Big] = -(-1)^{s(L)}\left(\frac{1}{\sqrt{2}}\right)^{c(L)}, \tag{4.8}$$

where $s(L)$ denotes the number of self-intersections and $c(L)$ counts the corners of the loop. One obtains

$$\begin{aligned}
\det\left[M^{[\phi]}\right] &= \prod_{\mathbf{n}} h^2(\mathbf{n}) \exp\left(\sum_{k=1}^{\infty}\frac{1}{2k}\sum_{\mathbf{m}}\sum_{L\in\mathcal{L}_{\mathbf{m}}^{(2k)}}\prod_{\mathbf{j}\in P(L)}\frac{1}{h(\mathbf{j})}(-1)^{s(L)}\left(\frac{1}{\sqrt{2}}\right)^{c(L)}\right)\\
Z_{GN} &= \int\prod_{\mathbf{n}}\left(\frac{\mathrm{d}\phi(\mathbf{n})}{\sqrt{2\pi g}}h^2(\mathbf{n})\,e^{-\frac{\phi^2(\mathbf{n})}{2g}}\right) \qquad (4.9)\\
&\quad\times\exp\left(\sum_{k=1}^{\infty}\frac{1}{2k}\sum_{\mathbf{m}}\sum_{L\in\mathcal{L}_{\mathbf{m}}^{(2k)}}\prod_{\mathbf{j}\in P(L)}\frac{1}{h(\mathbf{j})}(-1)^{s(L)}\left(\frac{1}{\sqrt{2}}\right)^{c(L)}\right).
\end{aligned}$$

Although now the partition function of the GN model looks more complicated at first glance, it is a great achievement that it is completely rewritten in terms of loops. At the moment the loops still appear in the exponent, but, by applying the hopping expansion to a so-called generalized 8-vertex model, it is possible to effectively expand the exponential function.

4.2 The generalized 8-vertex model

An 8-vertex model is defined by 8 vertices shown in Fig. 4.1. Each vertex is assigned a real weight $w_i,\ i = 1,\ldots,8$. Configurations are generated by covering the whole lattice with vertices as follows (compare [21, 22, 23] and for the generalized version [17]):
Each vertex is centered on a lattice point and the vertices are arranged in such a way that the lines on the vertices never have an open end. The Boltzmann factor is the product over the weights of all vertices in a configuration and the partition function is a sum over all allowed arrangements of the vertices.

In the generalized 8-vertex model the vertices are coupled to an external field $\varphi(\mathbf{n})$, which is located at the sites $\mathbf{n}$ of the lattice. Again, the partition

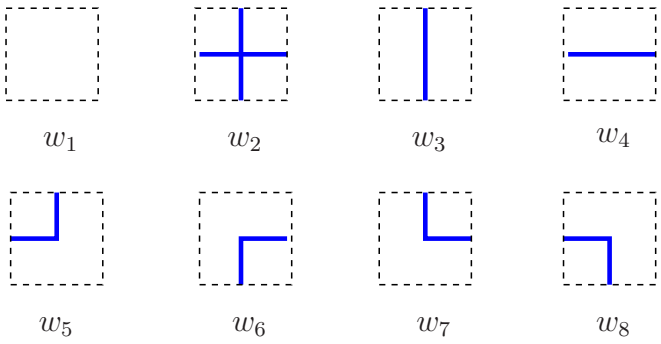

Figure 4.1: *8 vertices with their weights w_i.*

function is a sum over all admissible configurations $C \in \mathcal{C}$, but the Boltzmann weight obtains additional factors of the $\varphi(\mathbf{n})$: If a site $\mathbf{n}$ is occupied by one of the vertices 3 to 8, a factor of $\varphi(\mathbf{n})$ is taken into account. A factor of $\varphi(\mathbf{n})^2$ contributes to vertex 2 and for vertex 1 it is a factor of $\varphi(\mathbf{n})^0 = 1$. So the partition function for the generalized 8-vertex model reads

$$Z_{8v}(\varphi) = \sum_{C \in \mathcal{C}} \prod_{i=1}^{8} w_i^{n_i(C)} \prod_{\mathbf{n} \in \Lambda} \varphi(\mathbf{n})^{O(\mathbf{n})} \ , \tag{4.10}$$

where $n_i(C)$ denotes how often the vertex i occurs in the configuration C and $O(\mathbf{n})$ counts how many lines run through the site $\mathbf{n}$.

4.2.1 Grassmann representation

Now, the 8-vertex model is rewritten as an integral over Grassmann variables. To a lattice point $\mathbf{n}$ a set of 4 Grassmann variables $\eta_\mu(\mathbf{n})$, $\mu = \pm 1, \pm 2$ is assigned as shown in Fig. 4.2.
The action $S[\eta]$ consists of 3 terms: the hopping term $S_h[\eta]$, the monomer term $S_m[\eta]$ and the corner term $S_c[\eta]$ (see Fig. 4.3). $S_h[\eta]$ connects neighboring sites and thus, it represents the line elements of the loops. $S_m[\eta]$ and $S_c[\eta]$ determine in which way a loop continues at a site. The different loops are obtained by the differrent ways the Grassmann integral can be saturated, when expanding the exponential of the action.

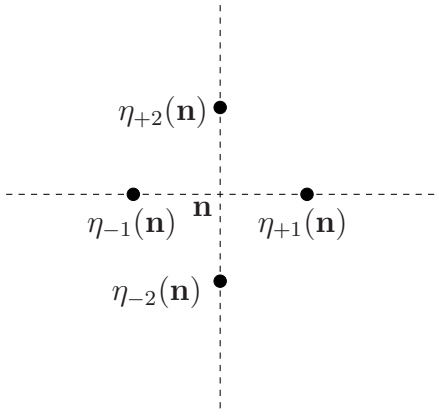

Figure 4.2: *Grassmann variables on the lattice. Actually, they all live on the lattice point. Only for a better visualization they are shifted apart.*

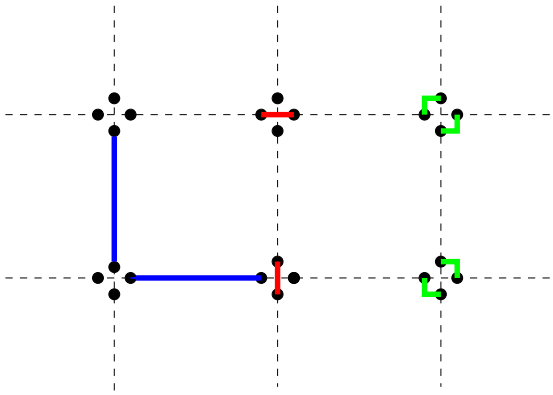

Figure 4.3: *Graphical representation of the hopping, monomer and corner terms of the action.*

Explicitly, the action reads

$$\begin{aligned}
S[\eta] &= S_h[\eta] + S_m[\eta] + S_c[\eta] \ , \\
S_h[\eta] &= a \sum_{\mathbf{n}\in\Lambda} \left[\eta_{\hat{1}}(\mathbf{n})\eta_{-\hat{1}}(\mathbf{n}+\hat{1}) + \eta_{\hat{2}}(\mathbf{n})\eta_{-\hat{2}}(\mathbf{n}+\hat{2})\right] \ , \\
S_m[\eta] &= \sum_{\mathbf{n}\in\Lambda} \left[b_3\ \eta_{-\hat{1}}(\mathbf{n})\eta_{\hat{1}}(\mathbf{n}) + b_4\ \eta_{-\hat{2}}(\mathbf{n})\eta_{\hat{2}}(\mathbf{n})\right] \ , \\
S_c[\eta] &= \sum_{\mathbf{n}\in\Lambda} \left[c_5\ \eta_{\hat{1}}(\mathbf{n})\eta_{-\hat{2}}(\mathbf{n}) + c_6\ \eta_{\hat{2}}(\mathbf{n})\eta_{-\hat{1}}(\mathbf{n}) \right. \\
&\qquad \left. + c_7\ \eta_{-\hat{2}}(\mathbf{n})\eta_{-\hat{1}}(\mathbf{n}) + c_8\ \eta_{\hat{2}}(\mathbf{n})\eta_{\hat{1}}(\mathbf{n})\right] \ ,
\end{aligned} \tag{4.11}$$

and the partition function for the Grassmann representation of the 8-vertex model is given by

$$Z_{Gv} = (-1)^{|\Lambda|} \int \prod_{\mathbf{n}\in\Lambda} \mathrm{d}\eta_{-\hat{2}}(\mathbf{n})\mathrm{d}\eta_{\hat{2}}(\mathbf{n})\mathrm{d}\eta_{-\hat{1}}(\mathbf{n})\mathrm{d}\eta_{\hat{1}}(\mathbf{n})\; e^{S[\eta]} \; . \tag{4.12}$$

When choosing $a = \sqrt{w_2}$, $b_i = -\frac{w_i}{\sqrt{w_2}}$ for $i = 3, 4$, and $c_i = -\frac{w_i}{\sqrt{w_2}}$ for $i = 5, \ldots, 8$, then integrating out the Grassmann variables reproduces Z_{8v}, i.e., $Z_{Gv} = Z_{8v}$. It has to be remarked that a necessary condition for the existence of a Grassmann representation is the *free fermion condition* [21]

$$w_1 w_2 + w_3 w_4 = w_5 w_6 + w_7 w_8 \; . \tag{4.13}$$

This is obeyed for the particular choice of weights w_i presented below.

4.2.2 Hopping expansion

Similar to the lattice GN model the Grassmann representation of the 8-vertex model can be expanded in the hopping term, as it is shown in detail in [17]. One obtains

$$Z_{8v} = (-1)^{|\Lambda|} w_1^{|\Lambda|} \; \exp\left(\frac{1}{2} \sum_{k=1}^{\infty} \frac{1}{2k} \sum_{\mathbf{n}\in\Lambda} \sum_{L\in\mathcal{L}_{\mathbf{n}}^{(2k)}} (-1)^{s(L)} \left(\frac{1}{w_1}\right)^{|L|} \right.$$
$$\left. \times \prod_{\mathbf{m}\in P(L)} \varphi(\mathbf{m}) \prod_{i=3}^{8} w_i^{n_i(L)} \right) \; . \tag{4.14}$$

In the last formula an extra factor $\frac{1}{2}$ appears in the exponent. This arises from the fact that the integral (4.12) of the quadratic action (4.11) gives rise to a Pfaffian, which is the square root of a determinant. The determinant in turn is obtained for bilinear actions such as (3.21). This implies that eventually Z_{8v} will have to be squared in order to reproduce Z_{GN}.

4.3 Fermion loop representation

The final step to reach the fermion loop representation of the GN model is to bridge the gap between the formulation of its partition function in hopping expansion and the partition function of the generalized 8-vertex model in hopping

expansion. This is done by a comparison of the two expressions and a suitable identification of the weights w_i. Comparing Eqs. (4.9) and (4.14) leads to the following conclusion: One uses a lattice with an even number of sites to get rid of the overall sign, w_1, w_3 and w_4 are chosen to be 1, w_5, w_6, w_7 and w_8 are set to $\frac{1}{\sqrt{2}}$, consequently, due to the free fermion condition w_2 equals 0, $\varphi(\mathbf{n})$ coincides with $\frac{1}{h(\mathbf{n})}$ and the whole term for the partition function is squared to obtain the determinant out of the Pfaffian. The fact that $w_2 = 0$ means that the vertex number 2 is absent and only self-avoiding loops occur. Taking into account the overall integration over ϕ, the final expression for Z_{GN} is given by

$$\begin{aligned} Z_{GN} &= \int \prod_{\mathbf{n}} \frac{\mathrm{d}\phi(\mathbf{n})}{\sqrt{2\pi g}} \left[\sum_{C \in \mathcal{C}} \left(\frac{1}{\sqrt{2}} \right)^{c(C)} \prod_{\mathbf{m}} \left[\frac{1}{h(\mathbf{m})} \right]^{J(C)} \right]^2 \prod_{\mathbf{n}} h^2(\mathbf{n}) \; e^{-\frac{1}{2g}\phi^2(\mathbf{n})} \\ &= \sum_{C_a, C_b \in \mathcal{C}} \left(\frac{1}{\sqrt{2}} \right)^{c(C_a)+c(C_b)} \prod_{\mathbf{n}} \int \frac{\mathrm{d}\phi(\mathbf{n})}{\sqrt{2\pi g}} e^{-\frac{1}{2g}\phi^2(\mathbf{n})} \left[h(\mathbf{n}) \right]^{2-J(\mathbf{n})} \; . \end{aligned} \tag{4.15}$$

From squaring Z_{8v} one obtains two independent sums over self-avoiding loops (C_a, C_b), which will be referred to as blue and red. $c(C_a)$ and $c(C_b)$ denote the numbers of corners for red and blue loops. $J(\mathbf{n})$ is the local occupation number of a site $\mathbf{n}$. $J(\mathbf{n}) = 2$, if a red and a blue loop run through $\mathbf{n}$, $J(\mathbf{n}) = 1$, if only one loop runs through $\mathbf{n}$ and $J(\mathbf{n}) = 0$ if the site is empty.
The integral over $\mathrm{d}\phi(\mathbf{n})$ can be solved explicitly. 3 different cases have to be considered:

- $J = 2$:
$$\int_{-\infty}^{\infty} \frac{\mathrm{d}\phi(\mathbf{n})}{\sqrt{2\pi g}} e^{-\frac{1}{2g}\phi^2(\mathbf{n})} = 1 \; , \tag{4.16}$$
- $J = 1$:
$$\int_{-\infty}^{\infty} \frac{\mathrm{d}\phi(\mathbf{n})}{\sqrt{2\pi g}} e^{-\frac{1}{2g}\phi^2(\mathbf{n})} [2 + m + \phi(\mathbf{n})] = 2 + m \; , \tag{4.17}$$
- $J = 0$:
$$\int_{-\infty}^{\infty} \frac{\mathrm{d}\phi(\mathbf{n})}{\sqrt{2\pi g}} e^{-\frac{1}{2g}\phi^2(\mathbf{n})} [2 + m + \phi(\mathbf{n})]^2 = (2 + m)^2 + g \; . \tag{4.18}$$

Thus, a factor of $2+m$ is produced whenever a site is single-occupied and a factor $(2 + m)^2 + g$ for an empty site. With n_1 counting the single-occupied sites and n_0 the empty ones, the partition function gets its final form:

$$Z_{GN} = \sum_{C} \left(\frac{1}{\sqrt{2}} \right)^{c_1} \left(\frac{1}{2} \right)^{c_2} (2 + m)^{n_1} \left((2 + m)^2 + g \right)^{n_0} \; . \tag{4.19}$$

Consistently, c_1 (c_2, resp.) is the number of sites occupied with one corner (two corners, resp.).

Since in the computer program a somewhat different notation is used, this notation is introduced as well. The factors f_1 and f_2 are defined as

$$f_1 = \frac{2+m}{(2+m)^2+g} \ , \qquad f_2 = \frac{1}{(2+m)^2+g} \ . \tag{4.20}$$

Taking into account that the amount of all empty, single-occupied and double-occupied vertices equals the number of sites, $|\Lambda| = n_0+n_1+n_2$, and by extracting a global factor $(1/f_2)^{|\Lambda|}$ out of the sum over all configurations in Z_{GN}, it is clear that Z_{GN} can alternatively be written as

$$Z_{GN} = \left(\frac{1}{f_2}\right)^{|\Lambda|} \sum_C \left(\frac{1}{\sqrt{2}}\right)^c {f_1}^{n_1} {f_2}^{n_2}. \tag{4.21}$$

n_2 consequentially denotes the number of double-occupied sites and c is the total amount of corners.

Chapter 5

Monte Carlo methods

Numerical simulations with Monte Carlo (MC) methods are a powerful tool in statistical physics (see, e.g., [24]). They enable one to compute physical observables for any parameter values in a non-perturbative way. Errors can be estimated and are systematically improvable by using more sample configurations and larger systems. MC methods can be applied to Lattice QFTs because these are also characterized by probability distributions. The fundamental idea of MC methods for calculating observables is to replace the set of all possible configurations by a smaller representative sample.

In this chapter the conceptual basis of the MC techniques, which can later be applied to the GN model, are presented.

5.1 Simple sampling vs. importance sampling

In general, expectation values of observables are defined as

$$\langle O \rangle = \int \mathrm{d}C \, P[C] O[C] \; , \tag{5.1}$$

where the integral runs over all possible configurations C, $O[C]$ are the observables and $P[C]$ are the probabilities responsible for the correct distribution of the configurations. These expectation values usually cannot be evaluated analytically - even not in the case when the configurations are discrete and the lattice is finite (as in the loop model). The reason is that already for small volumes the number of possible configurations becomes large. So, what means large? For the

loop model considered here, the variables of a single site can have 49 different values. Thus, in principle, one could have $49^{|\Lambda|}$ configurations. For an 8^2 lattice this is $49^{64} \approx 10^{128}$ configurations. Of course, many of these configurations violate the constraints (loops have to be closed) and cannot appear. Still, the number of legitimate configurations behaves as $c^{|\Lambda|}$ and a summation over all of them is out of the question. The MC method attacks this problem by approximating the expectation value, Eq. (5.1), with a finite number of configurations $C_n,\ n = 1, \ldots, N$:

$$\langle O \rangle \approx \bar{O} = \frac{1}{N} \sum_{n=1}^{N} O[C_n] P[C_n] \ . \tag{5.2}$$

If, as in Eq. (5.2), the C_n are chosen with equal weight, the method is called simple sampling. In Eq. (5.2) the C_n are reweighted with the probabilities $P[C_n]$, which here are given by

$$P[C_n] = \frac{1}{Z} e^{-S[C_n]} \ , \qquad Z = \sum_{n=1}^{N} e^{-S[C_n]} \ . \tag{5.3}$$

However, it turns out that most configurations are heavily suppressed by $P[C_n]$ and for distributions of the type (5.3) simple sampling is not suitable.

A more powerful method is importance sampling. With this method, the probability factors are already taken into account in the generation of the configurations. Hence, using importance sampling, Eq. (5.2) reduces to

$$\bar{O} = \frac{1}{N} \sum_{n=1}^{N} O[C_n] \ . \tag{5.4}$$

5.2 Markov chain

One way to implement importance sampling is to start with an arbitrary configuration $C^{(0)}$ and to generate a sequence of new configurations $C^{(n)}$, $n = 1, 2, \ldots$. This so-called Markov chain is characterized by a transition probability

$$T\left(C^{(n+1)} = C' \,|\, C^{(n)} = C\right) = T\left(C \longmapsto C'\right) \ . \tag{5.5}$$

An important property of a Markov chain is that the transition probability does not depend on the index n. The transition probabilities obey

$$0 \leq T\left(C \longmapsto C'\right) \leq 1 \qquad \text{and} \qquad \sum_{C'} T\left(C \longmapsto C'\right) = 1 \ . \tag{5.6}$$

In addition, the process has to be built such that it is ergodic, i.e., each configuration can be reached from any other configuration in a finite number of steps.

In equilibrium, the probability to jump into a configuration C' in a Markov step has to be equal to the probability to jump out of this configuration:

$$\sum_C T(C \longmapsto C')\, P[C'] = \sum_C T(C' \longmapsto C)\, P[C] \ . \tag{5.7}$$

The simplest solution of this equation is to fulfill the condition for each configuration C individually. This gives the *detailed balance condition*

$$T(C \longmapsto C')\, P[C'] = T(C' \longmapsto C)\, P[C] \ . \tag{5.8}$$

The algorithm presented below is based on that equation.

5.3 Metropolis algorithm

The Metropolis algorithm was introduced in 1953 by N. Metropolis, A. Rosenbluth, M. Rosenbluth, A. Teller and E. Teller [25]. It is an algorithm that solves the detailed balance condition (5.8) and works as follows:

1. Choose an initial configuration C.
2. Propose an arbitrary trial configuration $\tilde{C}$ near the current one.
3. Compute $\rho = \frac{P[\tilde{C}]}{P[C]}$.
4. Distinguish the two cases:
   - $\underline{\rho \geq 1 :}$
     Set $T(C \longmapsto \tilde{C}) = 1$ and accept the trial configuration $\tilde{C}$ as the new configuration C'. With $T(\tilde{C} \longmapsto C) = 1/\rho$ the detailed balance condition is fulfilled.
   - $\underline{\rho < 1 :}$
     To satisfy the detailed balance condition set $T(C \longmapsto \tilde{C}) = \rho$ and $T(\tilde{C} \longmapsto C) = 1$. In practice one draws a random number $r \in [0, 1)$. If $r \leq \rho$ the trial configuration is accepted as the new configuration C'.
5. Go back to (2.) as long as you want to update your system.

5.4 Error estimation

The statistical error σ made by the approximation in Eq. (5.2) can be calculated easily. An important technique is the Jackknife method [26, 27]. It works also for secondary observables, i.e., quantities that are composed of several simple observables or are obtained from a fit. In the following, such an observable is denoted by ω.

One first computes the expectation values of observables on a so-called Jackknife block of configurations, which is, e.g., the set of all configurations except the J-th one. Thus, there exist alltogether N Jackknife blocks (omitting the 1st, the 2nd, ..., the N-th configuration). The corresponding results for ω are denoted as $\omega^{(J)}, J = 1, \ldots, N$. One then computes

$$\bar{\omega} = \frac{1}{N} \sum_{J=1}^{N} \omega^{(J)} \qquad \text{and} \qquad \sigma_\omega^2 = (N-1) \sum_{J=1}^{N} \left(\bar{\omega} - \omega^{(J)} \right)^2 . \tag{5.9}$$

Finally, the resulting expectation value and its error are given by

$$\langle \omega \rangle = \bar{\omega} \pm \frac{\sigma_\omega}{\sqrt{N}} . \tag{5.10}$$

The statistical error of a calculation depends on the number of measurements N. According to the result (5.10), it is necessary to have fourfold statistics to halve the error.

Chapter 6

Algorithm for fermion loops

As was shown in Chap. 4, the GN model can be represented as a sum of loops. It is possible to simulate the model directly in the loop representation. A suitable algorithm faces the challenge to create and annihilate closed self-avoiding loops. Such an algorithm is presented in the following, initial conditions are analyzed and the arrangement of the measurements is discussed.

6.1 Structure of the computer program

The essential elements of the MC program developed in this diploma thesis are listed in the following and can be overviewed in Fig. 6.1: Before the actual algorithm can start, several preparations must be performed. The random generator "ranlux" has to be included [28, 29]. The arrays containing the neighborhood information (periodic boundary conditions are used here) have to be initialized and the input parameters like the lattice size, physical parameters (m, g), the number of measurements etc. must be specified. One has to decide in which initial configuration the algorithm should start. Three different initial conditions are discussed in Sec. 6.4. In general, the system is out of equilibrium at the beginning (due to the chosen initial conditions). Thus, the system has to be updated until it reaches equilibrium (see Sec. 6.5). Now the measurements may start. In particular the overall occupation numbers and those for single timeslices are computed and written to the outfiles. The calculation of observables built out of the occupation numbers is performed later in the analysis. There should be several updates between the individual measurements so that these are (almost)

uncorrelated. Afterwards the analysis program reads in the data produced by the MC program. It computes the expectation values of observables and their statistical errors with the Jackknife method (see Sec. 5.4).

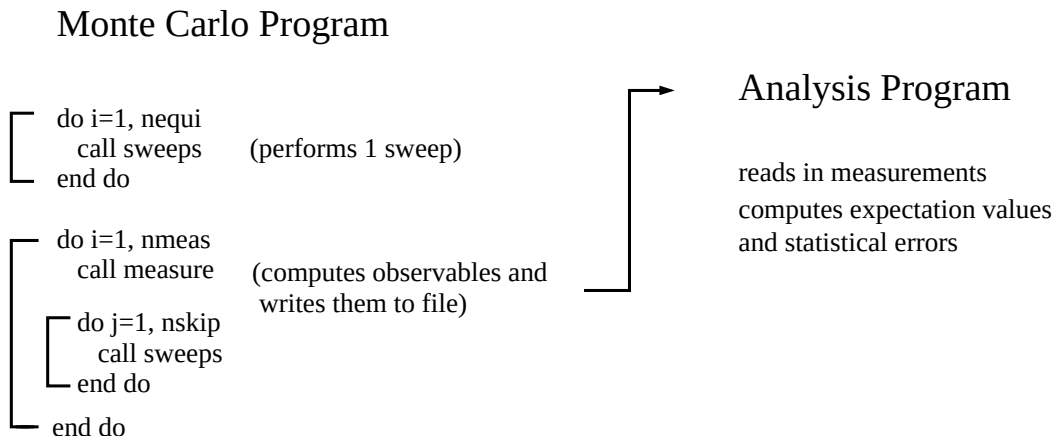

Figure 6.1: *Scheme of a MC program. A sweep means one update for each site, nequi is the number of sweeps needed to reach equilibrium, nmeas is the number of measurements and nskip denotes the number of sweeps between to measurements.*

6.2 How an update is implemented

The configurations of the model are loops living on the links of the lattice. Each link of the lattice can be empty, occupied by one loop or occupied by two different loops. A convenient visualization is to use different colors (red and blue) for the two types of loops. A legitimate configuration is one, where no self-intersections occur and neither red nor blue lines have an open end.

An example for a configuration of loops at $g = 0.5$ and $m = 0.1$ on a 64×64 lattice is shown in Fig. 6.2. Another way of thinking about a configuration is in terms of vertices. Vertices are plaquettes (minimal squares) of the dual lattice. They can be viewed as tiles put on the lattice, where each tile is centered at a site. The complete set of vertices is depicted in Fig. 6.3. The partition function is a sum over all possible arrangements of the vertices. Like in the 8-vertex model the vertices have characteristic weights. According to Eq. (4.21) on page 24, the weight factors are:

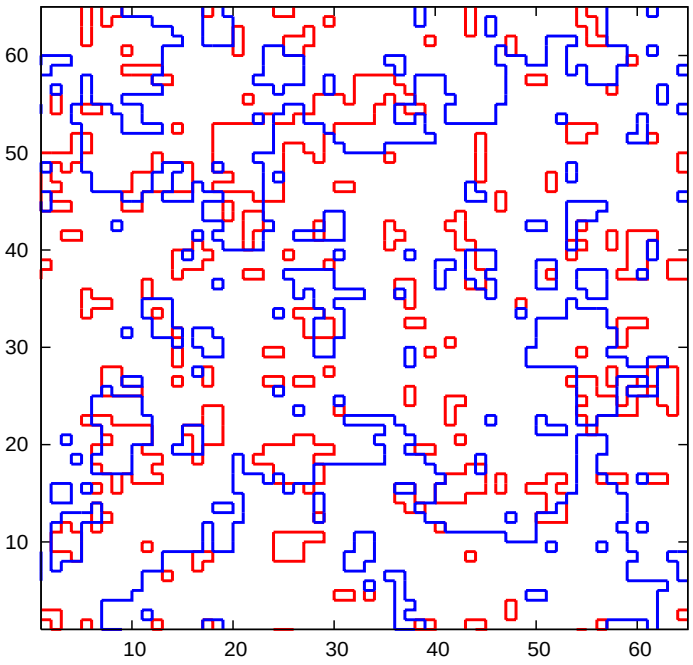

Figure 6.2: *Snap-shot of a loop configuration on a* 64×64 *lattice.*

- 1 for an empty vertex,
- f_1 for a vertex occupied by only one loop,
- f_2 for a vertex occupied by both loops,
- a factor of $\frac{1}{\sqrt{2}}$ for each corner,

where

$$f_1 = \frac{2+m}{(2+m)^2+g} \ , \qquad f_2 = \frac{1}{(2+m)^2+g} \ . \tag{6.1}$$

To obtain some feeling for the behavior of the weight factors f_1, f_2, their values are listed for a range of values m, g in Tab. 6.1.

As it was discussed in Sec. 5.3, in the Metropolis algorithm a trial configuration is generated and then accepted according to the change of the action it leads to. The trial configuration offered to the system has to be a legitimate one. Thus, it may not contain self-intersections or open loops. The simplest possibility to create a trial configuration is to invert a plaquette, i.e., every empty link of

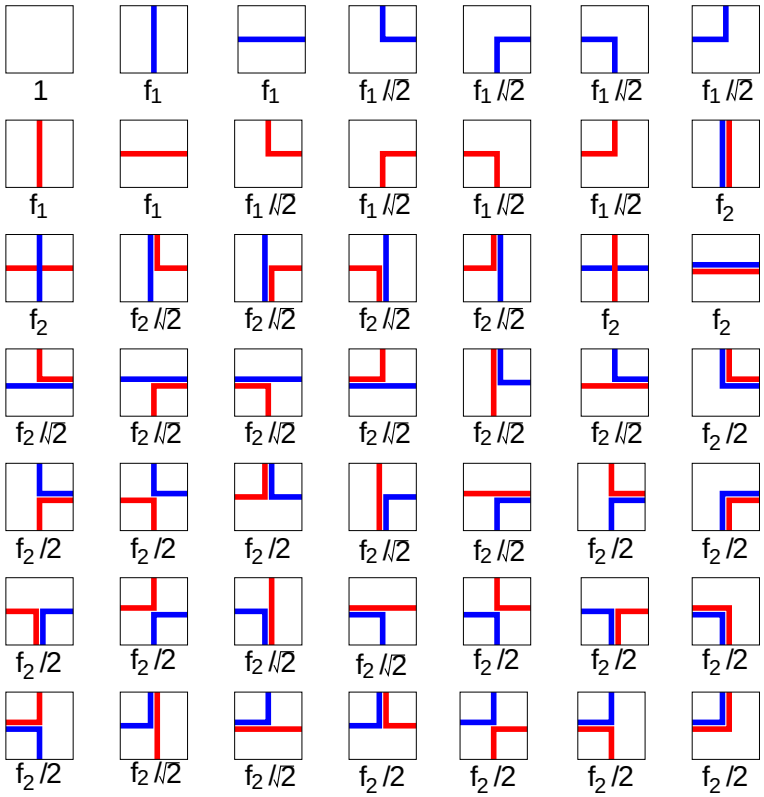

Figure 6.3: *The 49-vertex model. Configurations can be generated by putting representatives of these 49 tiles on the lattice, keeping in mind that loops must be closed and self-avoiding.*

g | m	-0.3	-0.15	0.0	0.15	0.3
0.0	$f_1 = 0.588$ $f_2 = 0.346$	$f_1 = 0.540$ $f_2 = 0.292$	$f_1 = 0.500$ $f_2 = 0.250$	$f_1 = 0.465$ $f_2 = 0.216$	$f_1 = 0.435$ $f_2 = 0.189$
0.1	$f_1 = 0.569$ $f_2 = 0.334$	$f_1 = 0.525$ $f_2 = 0.284$	$f_1 = 0.488$ $f_2 = 0.244$	$f_1 = 0.455$ $f_2 = 0.211$	$f_1 = 0.427$ $f_2 = 0.186$
0.3	$f_1 = 0.533$ $f_2 = 0.313$	$f_1 = 0.497$ $f_2 = 0.269$	$f_1 = 0.465$ $f_2 = 0.233$	$f_1 = 0.437$ $f_2 = 0.203$	$f_1 = 0.411$ $f_2 = 0.179$
0.5	$f_1 = 0.501$ $f_2 = 0.295$	$f_1 = 0.472$ $f_2 = 0.255$	$f_1 = 0.444$ $f_2 = 0.222$	$f_1 = 0.420$ $f_2 = 0.195$	$f_1 = 0.397$ $f_2 = 0.172$

Table 6.1: *Table of weight factors f_1, f_2 for various g and m.*

the plaquette becomes occupied and the other way round. Several examples of this step are illustrated in Fig. 6.4. This basic step is done individually for red and blue loops.

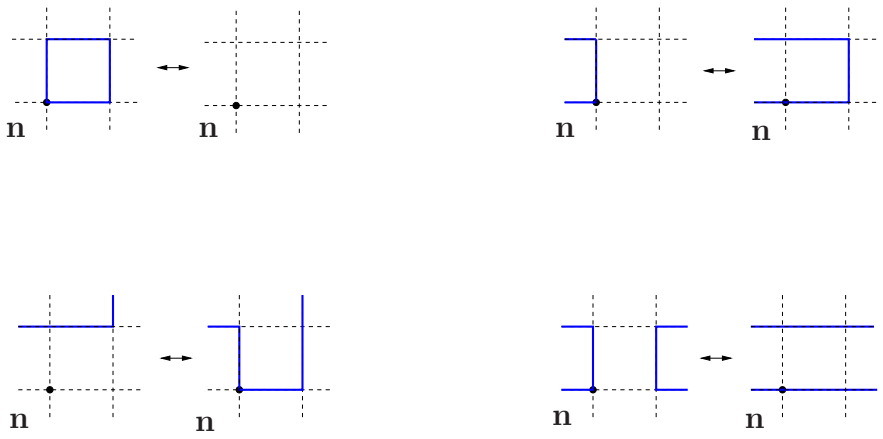

Figure 6.4: *Possible updates (no complete listing!) for one site by inverting a plaquette.*

Such an inversion is not admissible, if any site included in the plaquette has two occupied links, which do not belong to the plaquette. This case is shown in Fig. 6.5. Inverting such a plaquette would lead to forbidden vertices with two lines of the same color crossing each other. Thus, in the computer program this condition is checked explicitly and the update is rejected, if it would lead to a self-intersecting loop.

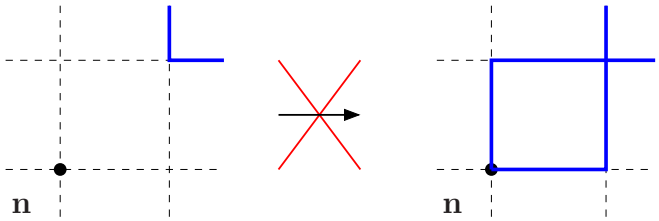

Figure 6.5: *If one of the corners in the direct vicinity of the plaquette is occupied, inverting the plaquette would lead to a forbidden self-intersection.*

Going through the whole lattice once and applying a MC update to each site is referred to as a "sweep". Due to the differently colored loops being independent from each other, the sweeps for the two colors are done alternately.

6.3 Ergodicity

As already announced in Sec. 5.2, a Markov chain MC algorithm has to be ergodic. If a so-called two-plaquette update is applied to the system in addition to the one-plaquette update (introduced in the previous section), it can be proven that the algorithm used here fulfills that criterion.

First, the distance d between two occupied links $o_\mu(\mathbf{m})$ and $o_\mu(\mathbf{n})$ lying in the same direction is defined as

$$d(o_\mu(\mathbf{m}), o_\mu(\mathbf{n})) \;=\; \begin{cases} |\mathrm{m}_\nu - \mathrm{n}_\nu|,\ \mu \neq \nu & \text{if } \mathrm{m}_\mu = \mathrm{n}_\mu \\ \mathrm{L}_\nu & \text{else .} \end{cases} \tag{6.2}$$

So, the minimal distance $D(C)$ of a configuration is given by

$$D(C) = \min\left[\, d(o_\mu(\mathbf{m}), o_\mu(\mathbf{n}))\,\right], \quad \mathbf{m}, \mathbf{n} \in \Lambda,\ \mu \in \{1, 2\}\ . \tag{6.3}$$

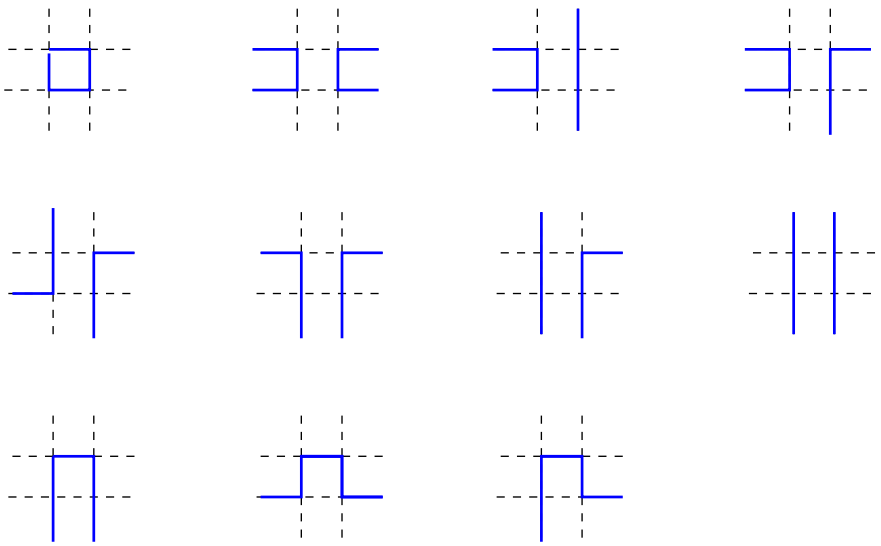

Figure 6.6: *Eleven types of configurations with minimal distance $D(C) = 1$.*

With this definition all possible configurations can be classified according to their minimal distance. Three categories need to be discussed:

1. $D(C) = 1$:
   There arise eleven types of configurations (see Fig. 6.6). Each of them can be created or annihilated with the one-plaquette update.

2. $D(C) \geq 3$:
   In this category there exist two types of configurations ("stairs" and "straight"), shown in Fig. 6.7, and combinations of them. Obviously, all of them can be updated by inverting one plaquette.

3. $D(C) = 2$:
   The possible configurations are of the same types as in category 2. Each configuration can be obtained and broken up with the one-plaquette update except the special case, where the complete configuration consists of "stairs", which cover the whole lattice. Here, no trial configuration can be provided, since there would occur self-intersections due to corners in the direct vicinity of the plaquette (see Sec. 6.2 and especially Fig. 6.5).

Figure 6.7: *Examples for types "stairs" and "straight" with minimal distance* $D(C) = 3$.

One way out of this special case presented in category 3 is to include a two-plaquette update, which allows to create and annihilate such a configuration of "stairs".

To summarize, one can say that the algorithm is ergodic, if both, one-plaquette and two-plaquette updates, are used. In this way each allowed configuration can be created and annihilated by the algorithm. In spite of this, the algorithm works with only one-plaquette updates in practice. The reason is that the 4 special configurations, which contain nothing else than "stairs", are of measure 0.

6.4 Initial conditions

Starting with an empty lattice, there is the possibility that a loop develops in the following way: As can be concluded from the two transitions on the right-hand side of Fig. 6.4, it can grow in one direction and finally meet with itself by closing around the periodic boundary of the lattice. Eventually, there arise two parallel

loops winding around the torus. It is easy to see that only even numbers of non-trivial loops can be generated (or annihilated) by the algorithm. To obtain an odd number, the initial configuration has to be changed by putting a non-trivially winding loop on the lattice by hand. Since there are loops of different colors, 4 different cases of simple initial configurations are possible:

1. Empty lattice: "even-even".
2. One non-trivial loop: "even-odd".
3. Two non-trivial loops of different color in the same direction: "odd-odd".
4. Two non-trivial loops of different color in different directions: "odd-odd".

Just as the empty lattice corresponds to an even number of non-trivial loops in each direction (sector of even-even boundary condition), the lattice with one non-trivial loop must have an even number of loops in one and an odd number of loops in the other direction (even-odd). For quadratic lattices [1] cases 3 and 4 are equivalent to each other due to the symmetry properties of the vertices (odd-odd).

As an example, the effect of different boundary conditions on observables is shown in Fig. 6.8, where the chiral condensate χ, which will be discussed in detail below, was computed on a 32^2-lattice. The plot includes the three different graphs for χ as a function of the mass parameter m, evaluated for the free case ($g = 0.0$). It is visible that there is no gap between the different graphs for small m at all. Only from about $m = -0.15$ on, the gap emerges and grows with increasing m. After $m = 0.1$ it remains constant. The explanation therefore is the following: The occupation densities are determinated by the weight factors for the vertices (see Fig. 6.3 and Eq. (6.1)), which in turn depend on the parameters m and g (see Tab. 6.1). In the interval $m \in [-0.3\,,\,0.3]$ used in Fig. 6.8, f_1 and f_2 are continuously decreasing for increasing m. This means that the occupation densities for single- and double-occupied vertices are decreasing as well (see Fig. 6.9). Consequently, the expectation values for occupation numbers do not change for different boundary conditions as long as m is so small that non-trivial loops do not dominate the system. With increasing m the system demands more and more empty vertices. Now, the non-trivial loops of the even-odd and the odd-odd cases interfere in the simulation because at least the last of them

[1] This is the case studied here.

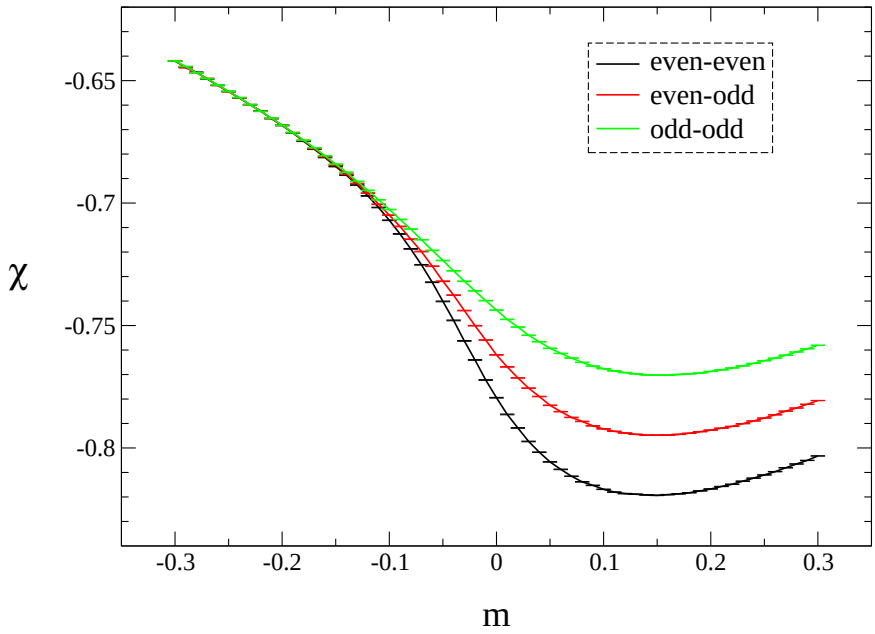

Figure 6.8: *Chiral condensate as a function of the mass parameter m for different initial conditions and coupling constant $g = 0.0$ on a 32×32 lattice.*

cannot be broken up. So, the non-trivial loop is the dominant contribution to the total occupation. In the end, when m is greater than about 0.1, the whole lattice would almost be unoccupied according to the weight factors. With one or two non-trivial loops lying on the lattice, the gap between the data of different boundary conditions roughly corresponds to the number of links occupied by the non-trivial loops. This number amounts to the length of the lattice. For sufficiently large m the occupation rules do no longer differ from 0 substantially and this finite size effect remains constant if m is increased further.

The above observation allows to understand the leading finite volume effect from different boundary conditions. Most obvious is the limit for large m (in the free case), when the lattice prefers an unoccupied state. L links are forced to be occupied for the even-odd sector, so one can estimate the ratio of constrained sites to correctly occupied (i.e., empty) sites as $\frac{L}{L^2-L} \approx \frac{1}{L}$, where L denotes the length of a quadratic lattice and L^2 the total number of lattice points.

A more generalized formula, which is less phenomenological, can be derived for every value of m by ignoring the microscopic behavior and parameterizing the occupation in terms of densities. This approach to understanding the finite size

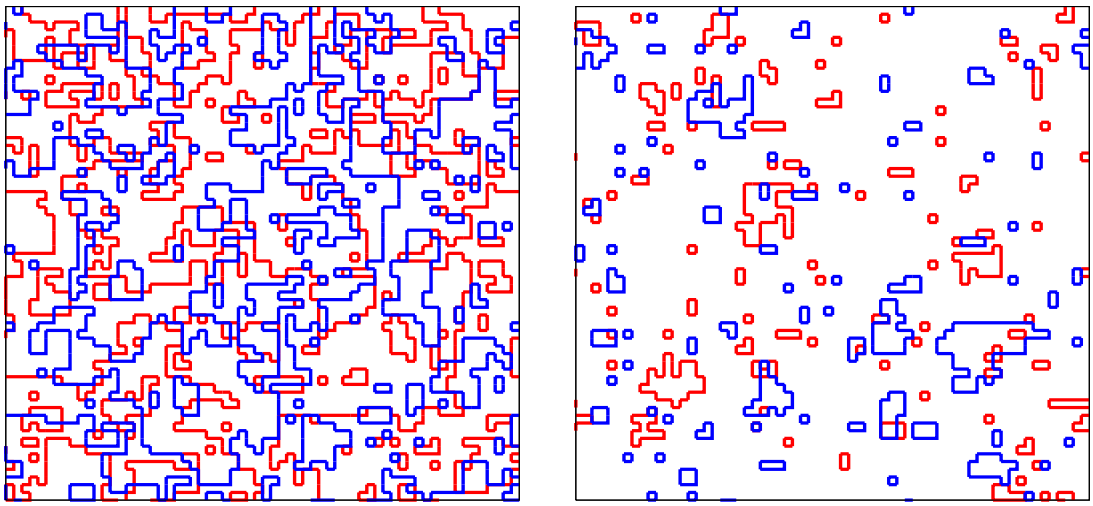

(a) $m = -0.2$ (b) $m = 0.1$

Figure 6.9: *Typical loop configurations on a* 64×64 *lattice* ($g = 0.0$).

effects is in the spirit of the mean-field approximation.

Let $\sigma_0(m, g)$ be the density of empty sites, $\sigma_1(m, g)$ the density of single-occupied and $\sigma_2(m, g)$ the one of double-occupied sites in equilibrium. The sum rule $\sigma_0 + \sigma_1 + \sigma_2 = 1$ is evident. Then the total number of empty and single-occupied sites for the even-even (ee) sector is given by

$$n_0^{(\mathrm{ee})} = L^2\,\sigma_0(m, g)\ , \qquad n_1^{(\mathrm{ee})} = L^2\,\sigma_1(m, g)\ . \tag{6.4}$$

The densities σ can be rewritten in terms of occupation probabilities for red (p_R) and blue (p_B) loops:

$$\sigma_0 = (1 - p_R)(1 - p_B)\ , \tag{6.5}$$

$$\sigma_1 = p_R(1 - p_B) + p_B(1 - p_R) = p_R + p_B - 2p_R p_B\ , \tag{6.6}$$

$$\sigma_2 = p_R p_B\ . \tag{6.7}$$

Inserting the right-hand side of Eq. (6.7) into Eq. (6.6), there results

$$2\sigma_2 + \sigma_1 = p_R + p_B\ . \tag{6.8}$$

For the even-odd (eo) sector, one gets the following equations (with Eqs. (6.5) and (6.8)), as here, L sites (those of the non-trivial loop) are occupied by one

color at least:

$$\begin{aligned} n_0^{(\mathrm{eo})} &= (L^2 - L)\,\sigma_0 \ , \\ n_1^{(\mathrm{eo})} &= (L^2 - L)\,\sigma_1 + \frac{L}{2}(1 - p_R + 1 - p_B) \\ &= L^2\,\sigma_1 - \frac{L}{2}\sigma_1 + L\sigma_0 \ . \end{aligned} \tag{6.9}$$

The formula for the chiral condensate χ, which will be introduced in Chap. 7, Eq. (7.3), reads

$$\chi = -\frac{1}{L^2}\left[\frac{f_2}{f_1}\langle\, n_1 \,\rangle + 2f_1\langle\, n_0 \,\rangle\right] \ , \tag{6.10}$$

and so, the difference of χ between the two sectors can be computed:

$$\begin{aligned} \Delta\chi^{(\mathrm{eo-ee})} &= \chi^{(\mathrm{eo})} - \chi^{(\mathrm{ee})} \\ &= \frac{1}{L}\left[\frac{f_2}{f_1}\left(\frac{1}{2}\sigma_1 - \sigma_0\right) + 2f_2\sigma_0\right] \ . \end{aligned} \tag{6.11}$$

For the distance between the even-even and the odd-odd (oo) sector, one obtains a similar equation:

$$\Delta\chi^{(\mathrm{oo-ee})} = \chi^{(\mathrm{oo})} - \chi^{(\mathrm{ee})} = \frac{1}{L}\left[\frac{f_2}{f_1}\,(\sigma_1 - 2\sigma_0) + 4f_2\sigma_0\right] = 2\Delta\chi^{(\mathrm{eo-ee})} \ . \tag{6.12}$$

Thus, the finite size discrepancy between the oo and ee sector is twice as big as the effect between the eo and ee one. Most significant is that the leading terms of order $O(L^0)$ cancel out each other and so the subleading terms of order $O(L^{-1})$ govern the behavior of the finite size effect.

The amplitude in front of the $\frac{1}{L}$ behavior is not universal. This can be seen in the limit, where f_1 and f_2 become small. The density σ_1 vanishes and σ_0 approaches 1. One finds

$$\Delta\chi^{(\mathrm{eo-ee})} = -\frac{1}{L}\,\frac{f_2}{f_1} = -\frac{1}{L}\,\frac{1}{2+m} \ . \tag{6.13}$$

Since $f_1 = \frac{2+m}{(2+m)^2+g}$ and $f_2 = \frac{1}{(2+m)^2+g}$, f_1 and f_2 can be set to 0 by letting $g \to \infty$. Eq. (6.13) shows that the amplitude of the $\frac{1}{L}$ term can assume arbitrary values if one adjusts m. Hence, the conclusion is (as mentioned) that the amplitude of the finite size effect is not universal.

One can try to estimate σ_0 and σ_1 as the density of empty and single occupied vertices on the largest lattice which is computed. This is a crude estimate,

since microscopic details are neglected in the derivation of Eqs. (6.11) and (6.12), but worth a try. On a 700^2 lattice one obtains for the $\sigma_i(m,g)$

$$\begin{aligned} \sigma_0(0.1,0.0) &\approx 0.74 \ , \qquad \sigma_1(0.1,0.0) \approx 0.24 \ , \\ \sigma_0(0.1,0.1) &\approx 0.77 \ , \qquad \sigma_1(0.1,0.1) \approx 0.21 \ . \end{aligned} \tag{6.14}$$

Inserting the numbers into (6.11) and (6.12), one finds

$$\Delta\chi^{(\mathrm{eo-ee})} = \frac{1}{L} \begin{cases} 0.41 \text{ for } g = 0.0 \\ 0.40 \text{ for } g = 0.1 \end{cases} \ , \tag{6.15}$$

and

$$\Delta\chi^{(\mathrm{oo-ee})} = \frac{1}{L} \begin{cases} 0.82 \text{ for } g = 0.0 \\ 0.80 \text{ for } g = 0.1 \end{cases} \ . \tag{6.16}$$

A fit to the actual finite size behavior performed in Sec. 8.2 (compare Tab. 8.2) gives

$$\Delta\chi^{(\mathrm{eo-ee})} = \begin{cases} 0.86 \, \dfrac{1}{L^{0.99}} \text{ for } g = 0.0 \\ 0.72 \, \dfrac{1}{L^{0.96}} \text{ for } g = 0.1 \end{cases} \ , \tag{6.17}$$

and

$$\Delta\chi^{(\mathrm{oo-ee})} = \begin{cases} 1.85 \, \dfrac{1}{L^{1.00}} \text{ for } g = 0.0 \\ 1.47 \, \dfrac{1}{L^{0.97}} \text{ for } g = 0.1 \end{cases} \ . \tag{6.18}$$

Obviously, the discrepancy between the true physics and the results from the mean-field-type arguments is sizeable and shows the limitations of the mean-field approach. The $\frac{1}{L}$ behavior (see Sec. 8.2) and the relative factor of 2 between the eo-ee and the oo-ee finite size effects are predicted correctly, while the overall amplitude depends on microscopic details.

6.5 Equilibration

In order to get correct results, the system has to be updated until it is completely in equilibrium. The required period of MC time, the so-called equilibration time, can be found by monitoring observables for each sweep. As soon as the signal does not change anymore beyond fluctuations, equilibrium is reached.

Here, basic observables are used for studying equilibration: the density of empty vertices, of single occupation and of corners. Their histories as a function

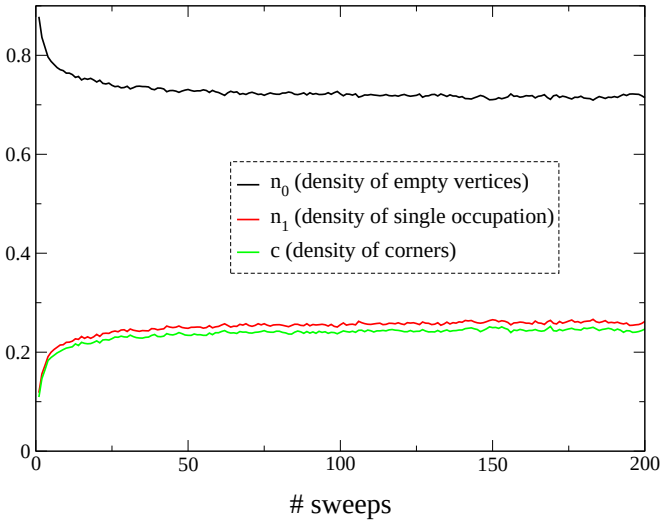

Figure 6.10: *Density n_0 of empty vertices, n_1 of single occupation and c of corners as a function of the number of sweeps at $m = -0.3$ and $g = 0.0$ on a 256^2 lattice.*

of the number of sweeps are shown in Fig. 6.10 for a given set of parameters m, g on a 256^2 lattice. It is obvious that for this case the system reaches equilibrium after about 100 sweeps. Of course, the rate of equilibration will depend on the values of the parameters and the volume. These effects are demonstrated in Figs. 6.11 and 6.12.

In Fig. 6.11 the single occupation density is compared for different mass parameters m (l.h.s. plot) and coupling constants g (r.h.s. plot). With increasing m correlations become more short-ranged and hence, the equilibration time decreases. A similar effect appears for changing the coupling: increasing g reduces the equilibration time.

In Fig. 6.12 the effect of the volume on the equilibration is studied for fixed g and m. As expected, smaller systems show larger fluctuations and thus equilibrate much faster. On larger lattices self averaging reduces the fluctuations. Also it takes longer for an excitation to propagate through a large lattice and consequently, the equilibration time increases.

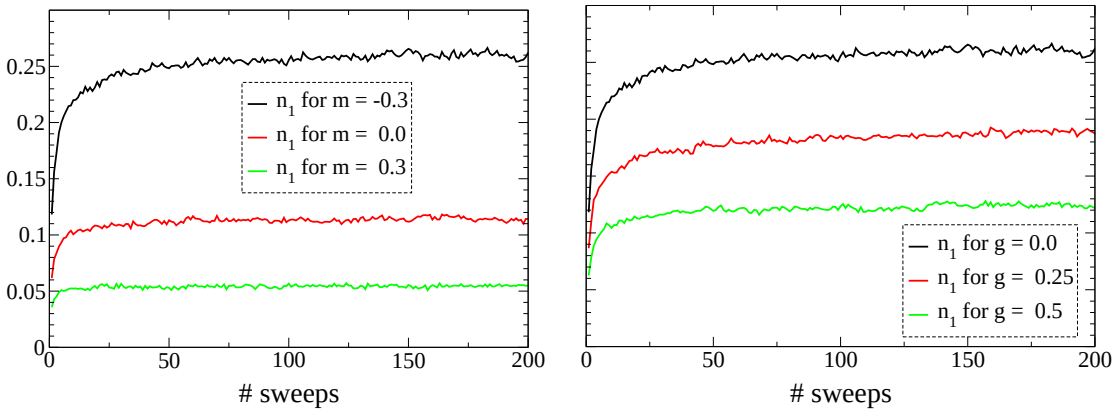

Figure 6.11:

Left-hand side: *Density n_1 of single occupation for various mass parameters m at $g = 0.0$ on a 256^2 lattice.*

Right-hand side: *Density n_1 of single occupation for various coupling parameters g at $m = -0.3$ on a 256^2 lattice.*

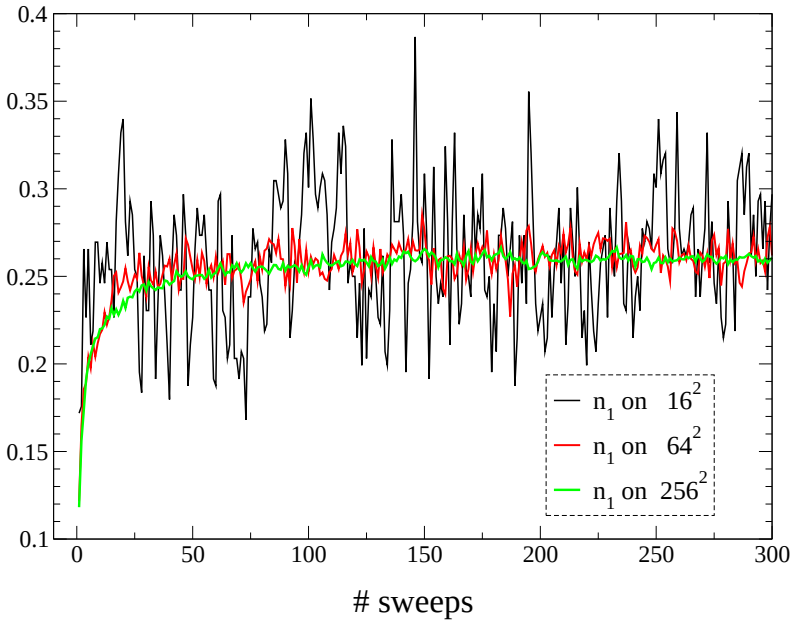

Figure 6.12: *Density n_1 of single occupation for various lattice sizes at $g = 0.0, m = -0.3$.*

Chapter 7

Bulk Observables

The fastest way to check if a new algorithm runs correctly is to compare some observables which are easy to evaluate with the results from the established methods or results from the analytic solution at $g = 0$, which can be obtained using Fourier transformation. Particularly useful observables are derivatives of the partition function

$$Z_{GN} = \sum_C \left(\frac{1}{\sqrt{2}}\right)^c (2+m)^{n_1} \left((2+m)^2 + g\right)^{n_0} \ . \tag{7.1}$$

Such derivatives are often referred to as "bulk observables".

In this chapter several bulk observables are presented and discussed. They will be compared to analytic results and to those from the standard approach in Chap. 9.

7.1 Chiral condensate and mass susceptibility

In terms of the familiar Grassmann representation the chiral condensate χ is given by

$$\chi = \frac{1}{|\Lambda|} \sum_{\mathbf{n}} \langle \bar{\psi}(\mathbf{n}) \psi(\mathbf{n}) \rangle \ . \tag{7.2}$$

The underlying expression is proportional to the derivative of the free energy $\ln Z_{GN}$ with respect to m. Applying this to the fermion loop representation, one obtains

$$\chi = -\frac{1}{|\Lambda|} \frac{\partial \ln Z_{GN}}{\partial m} = -\frac{1}{|\Lambda|} \left[\frac{f_2}{f_1} \langle\, n_1 \,\rangle + 2 f_1 \langle\, n_0 \,\rangle \right] \ . \tag{7.3}$$

Its derivative with respect to m, the so-called mass susceptibility C_χ, reads

$$
\begin{aligned}
C_\chi &= \frac{1}{|\Lambda|}\frac{\partial}{\partial m}\sum_{\mathbf{n}}\langle\bar{\psi}(\mathbf{n})\psi(\mathbf{n})\rangle = -\frac{1}{|\Lambda|}\frac{\partial^2 \ln Z_{GN}}{\partial m^2} \qquad (7.4)\\
&= -\frac{1}{|\Lambda|}\left\{\left[4{f_1}^2 - 2f_2\right]\left\langle(n_0 - \langle\, n_0\,\rangle)^2\right\rangle + \left[\left(\frac{f_2}{f_1}\right)^2 - 2f_2\right]\left\langle(n_1 - \langle\, n_1\,\rangle)^2\right\rangle\right.\\
&\quad \left. + 2f_2\left\langle(n_0 + n_1 - \langle\, n_0 + n_1\,\rangle)^2\right\rangle - \left[4{f_1}^2 - 2f_2\langle\, n_0\,\rangle - \left(\frac{f_2}{f_1}\right)^2\right]\langle\, n_1\,\rangle\right\}.
\end{aligned}
$$

Here, the expectation values are written as fluctuations in order to keep the computer errors, which result from finite precision, as small as possible. For analyzing the bulk observables several simulations ran for different lattice sizes and parameter values.

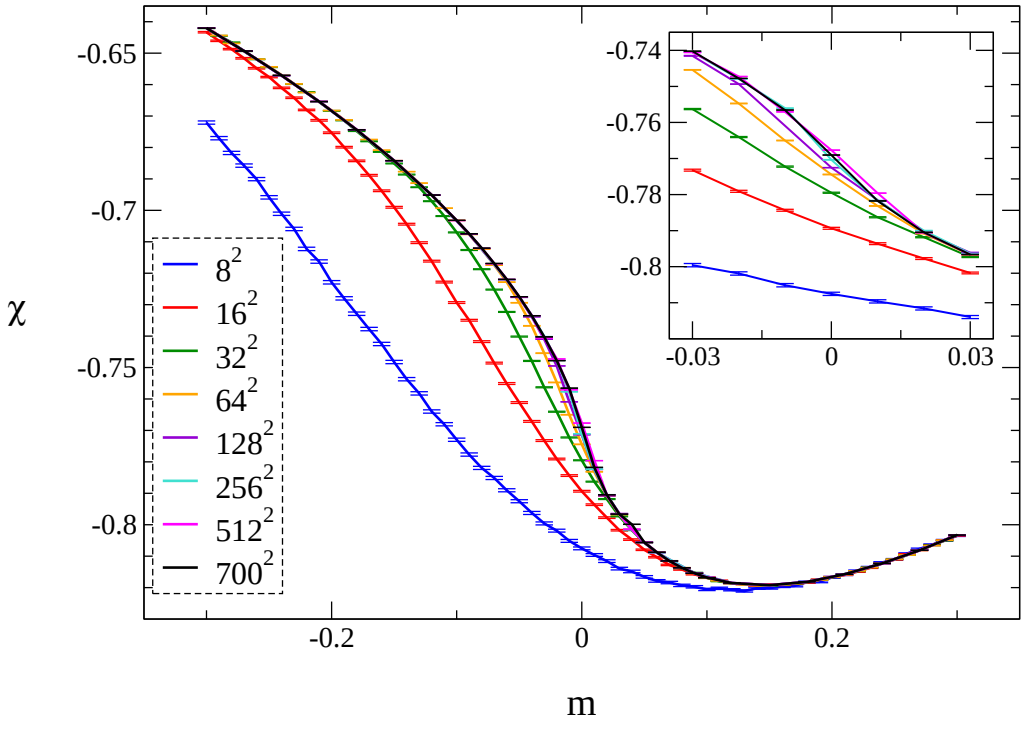

Figure 7.1: *Chiral condensate as a function of the mass parameter m for different lattice sizes in the free case ($g = 0.0$).*

Fig. 7.1 shows the chiral condensate as a function of the mass parameter m for the free case calculated in the fermion loop representation on different volumes. The initial configuration always was the empty lattice. The main conclusion of this picture is that the difference between different lattice sizes diminishes more and more with increasing volume, except at the critical value $m = 0.0$. This finite size effect will be discussed in detail below.

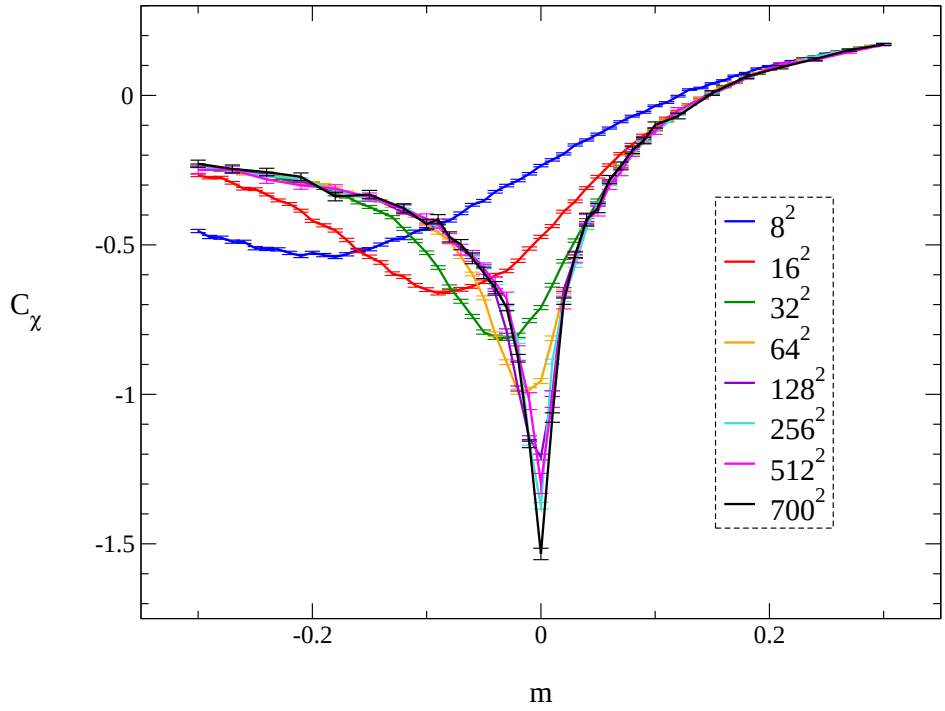

Figure 7.2: *Mass susceptibility as a function of the mass parameter m for different lattice sizes in the free case ($g = 0.0$).*

An equivalent figure was produced for the mass susceptibility (Fig. 7.2). One can see that the discrepancy between the data sets vanishes slower, especially in the critical region around $m = 0.0$. It seems as if there was a delta function in the continuum limit and a kind of phase transition or cross-over is emerging for the mass susceptibility. However, from a lattice size of about 256^2 on (for a precise analysis see Sec. 8.1), the extremum of the susceptibility does not decrease further. The minimum of the data set for the 512^2 lattice is less pronounced than the one for the 256^2 lattice. Probably, this fact results from autocorrelation. As

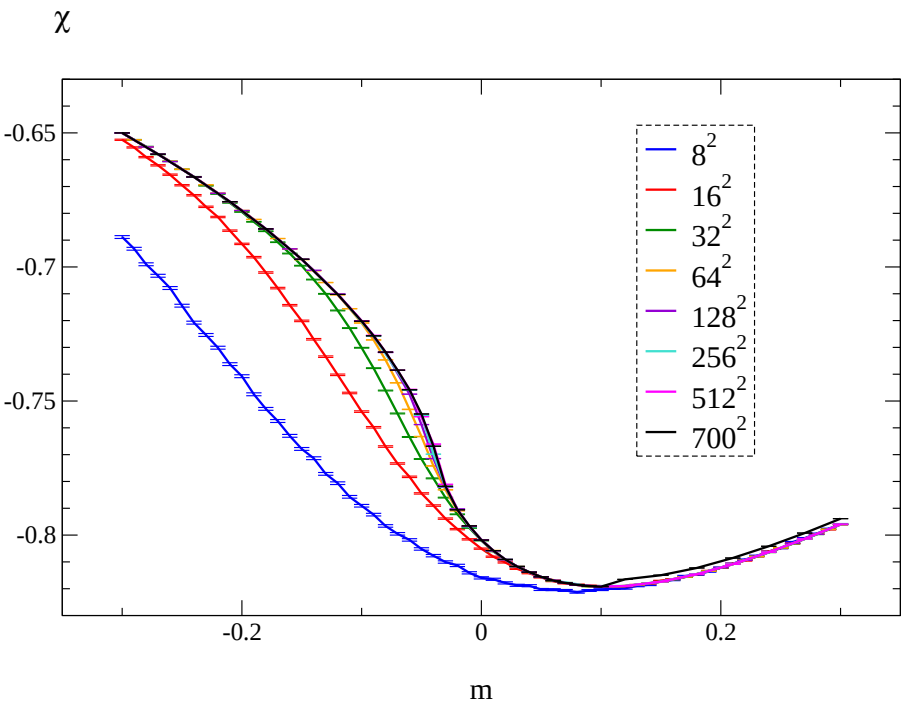

Figure 7.3: *Chiral condensate as a function of the mass parameter m for different lattice sizes at coupling $g = 0.1$.*

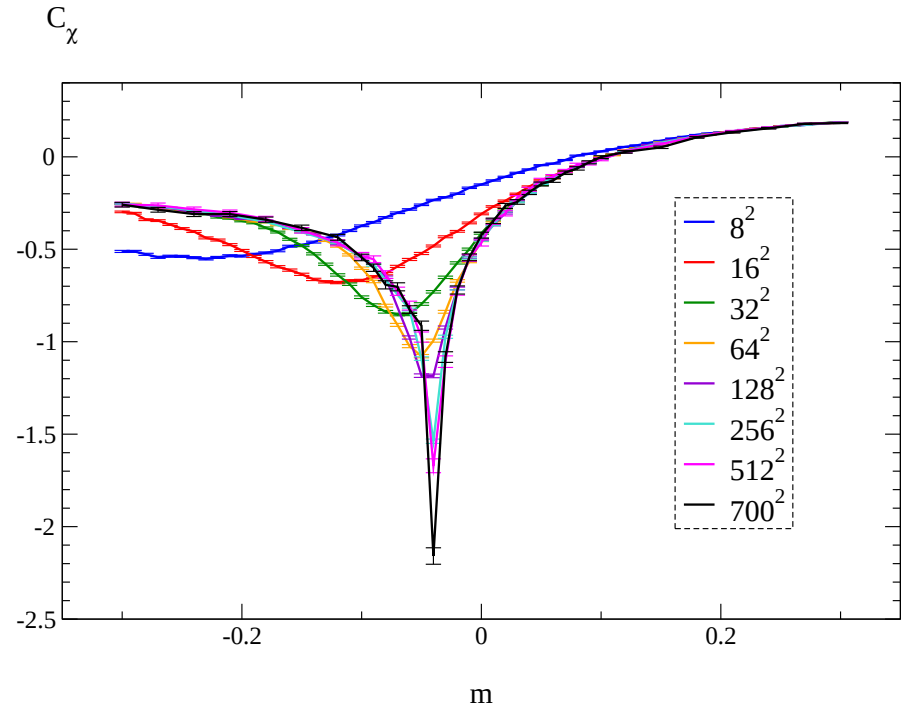

Figure 7.4: *Mass susceptibility as a function of the mass parameter m for different lattice sizes at coupling $g = 0.1$.*

the algorithm for fermion loops only uses one-plaquette updates, excitations need a longer time to propagate through the entire lattice with increasing the size of the system. Hence, it is supposed that the systematical error of calculations on very large lattices is notable.

The chiral condensate and the mass susceptibility for $g = 0.1$ are plotted in Figs. 7.3 and 7.4. Compared to the free case, the curve for χ seems to have the same shape at first glance. But regarding the "peak" in C_χ, there arises a contrast: Its minimum is shifted from $m = 0.0$ to $m \approx -0.04$ and with enlarging the lattice size the peak becomes more and more pronounced without any slowing down. A turned on coupling means that the acceptance for loops on the lattice decreases. So, a crude assumption is that the autocorrelation time might decrease with the density of occupied links.

7.2 Interaction density and interaction susceptibility

The interaction density ρ is defined as

$$\rho = \frac{1}{|\Lambda|} \sum_{\mathbf{n}} \left\langle \left(\bar{\psi}(\mathbf{n}) \psi(\mathbf{n}) \right)^2 \right\rangle = 2 \, \frac{1}{|\Lambda|} \, \frac{\partial \ln Z_{GN}}{\partial g} = \frac{2}{|\Lambda|} \, f_2 \, \langle \, n_0 \, \rangle \ , \tag{7.5}$$

and its derivative with respect to g, the interaction susceptibility C_ρ, is given by

$$C_\rho = \frac{4}{|\Lambda|} \, \frac{\partial^2 \ln Z_{GN}}{\partial g^2} = \frac{4}{|\Lambda|} \, {f_2}^2 \left[\left\langle \, (n_0 - \langle \, n_0 \, \rangle)^2 \, \right\rangle - \langle \, n_0 \, \rangle \right] \ . \tag{7.6}$$

Again, these two bulk observables were calculated on several volumes for the free and the coupled case as a function of the mass parameter (see Fig. 7.5). Their graphs behave similar to the graphs for the chiral condensate and its derivative. For the susceptibilities one obtains a straight convergence of the peak in the coupled case, whereas in the free case the maximum values of the peaks do not grow further for large lattice sizes.

7.3 Phase transition / Cross-over

For an infinite system, first order phase transitions are delta functions in the susceptibility. In finite systems these delta functions are melting into continuously

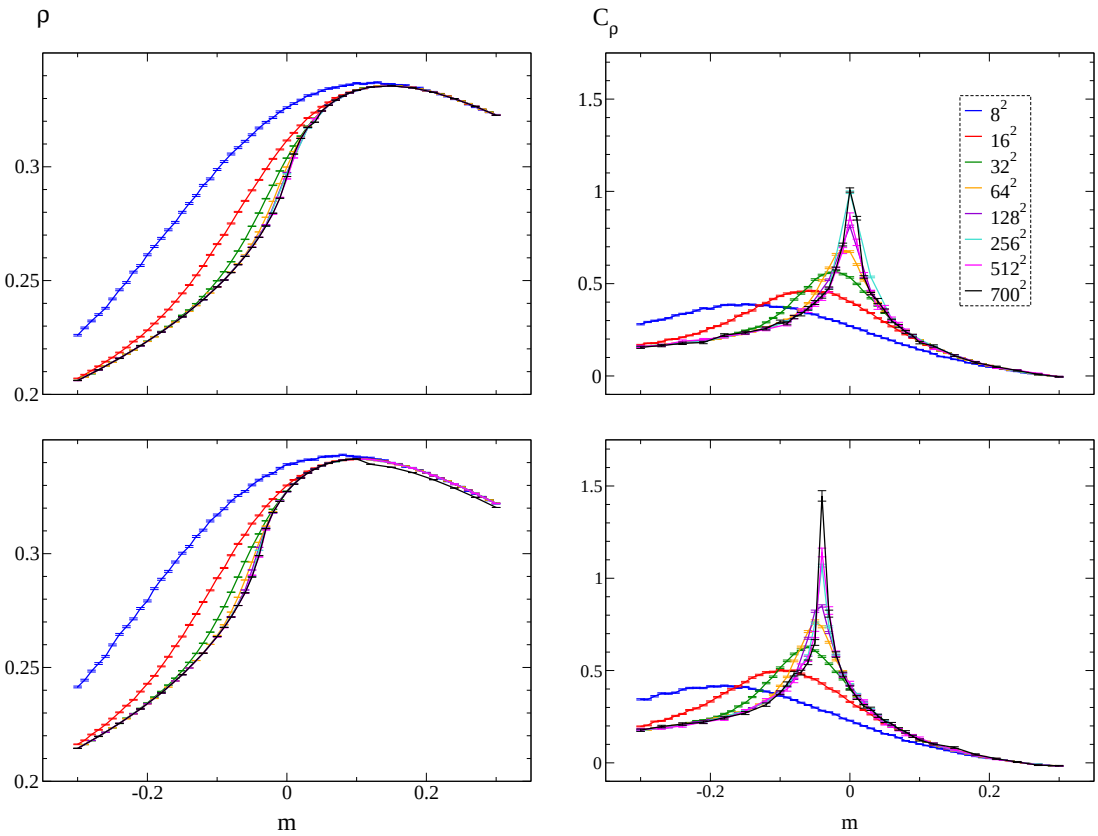

Figure 7.5:

Top left: ρ *as a function of* m *for different lattice sizes at* $g = 0.0$.

Top right: C_ρ *as a function of* m *for different lattice sizes at* $g = 0.0$.

Bottom left: ρ *as a function of* m *for different lattice sizes at coupling* $g = 0.1$.

Bottom right: C_ρ *as a function of* m *for different lattice sizes at coupling* $g = 0.1$.

differentiable functions, which have a pronounced extremum near the transition point. If the height of such peaks behaves proportional to L^d (with d being the dimension of the system) and the width of the peak is proportional to L^{-d}, then the phase transition is identified as a first order phase transition (see [24, 30]). For second order transitions there exists a critical exponent α, which governs the behavior of the height of the peak with enlarging the system. Otherwise, when no such exponent exists, the system has a cross-over.

It can be concluded from the plots of the chiral condensate and especially the mass susceptibility that there is a kind of phase transition or cross-over at $m = 0.0$ for the free case and near $m = -0.04$ for $g = 0.1$. The curvature of χ

changes and C_χ might indicate a divergence in the continuum limit.

To examine if it is a transition of first or higher order, one analyzes histograms of the measured values for observables using small intervals (bins), e.g., of length $2.5 \cdot 10^{-4}$, around the critical region. A two-state signal with a local minimum in-between gives evidence for a first order transition, where near the transition point two phases compete with each other. An approximately Gaussian shape of the histograms hints at a higher order transition or a cross-over.

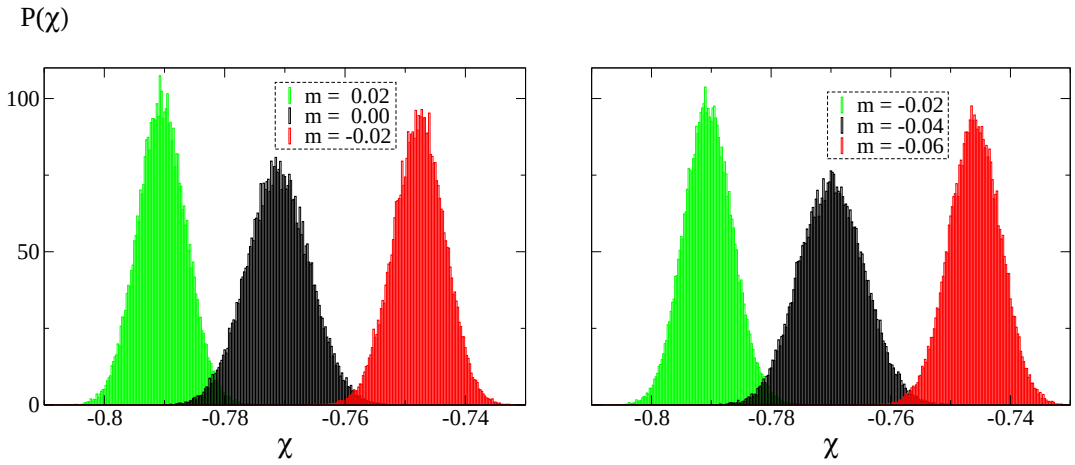

Figure 7.6: *Histograms for the frequency of measured values of χ on a 256^2 lattice.*

Left-hand side: *Free case (critical value: $m = 0.0$).*

Right-hand side: *Coupled case at $g = 0.1$ (critical value: $m = -0.04$).*

Fig. 7.6 shows the histograms for the chiral condensate on a 256^2 lattice for $m = -0.02, 0.0$ and 0.02 in the free case (l.h.s. plot) and for $m = -0.06, -0.04$ and -0.02 in the coupled case at $g = 0.1$ (r.h.s. plot). Since the shapes of the black histograms with the critical parameter values $m = 0.0$ and $m = -0.04$ do not differ essentially from the other ones, it follows that the peaks in the second derivatives of the free energy are not related to first order transitions.

The decision between a second order transition and a cross-over cannot be made with the bulk observables considered here because to examine critical exponents would demand to compute the specific heat

$$C_S = \frac{1}{|\Lambda|} \left(\langle S^2 \rangle - \langle S \rangle^2 \right) \ . \tag{7.7}$$

Chapter 8

Finite size effects

Since a computer is finite, one is forced to simulate on finite volumes. As long as the system feels the boundaries, one encounters finite size effects. With enlarging the volume, finite size effects will decrease in general. There are two types of finite size effects discussed in this work. The first one is a study of the volume scaling of the mass and the interaction susceptibility at their extremal values, the second one concerns the use of different boundary conditions.

8.1 Extrema of the susceptibilities

Following the ideas discussed in Sec. 7.3, the behavior of the susceptibilities C_χ and C_ρ is analyzed to examine if there are nonanalyticities in the derivatives of the free energy. As all simulations have to run on finite lattices, sharp delta functions can no longer occur. In fact, they are rounded and shifted over some region, which shrinks smoothly to zero with enlarging the system. Another finite size effect is the height of their peaks, studied below.

It can already be seen in the graphs for the susceptibilities (Fig. 7.2, 7.4 and 7.5) that the height of the peaks increases with enlarging the lattice size. The detailed analysis is presented in Figs. 8.1 and 8.2, where the minimum of the chiral susceptibility and the maximum of the interaction susceptibility are plotted against the lattice size. The data points beyond the 128^2 lattice are not considered in the free case because there, the computation is strongly affected by autocorrelation. As announced, this effect results from the local algorithm, which only applies one-plaquette updates to the system. Therewith, the systematic

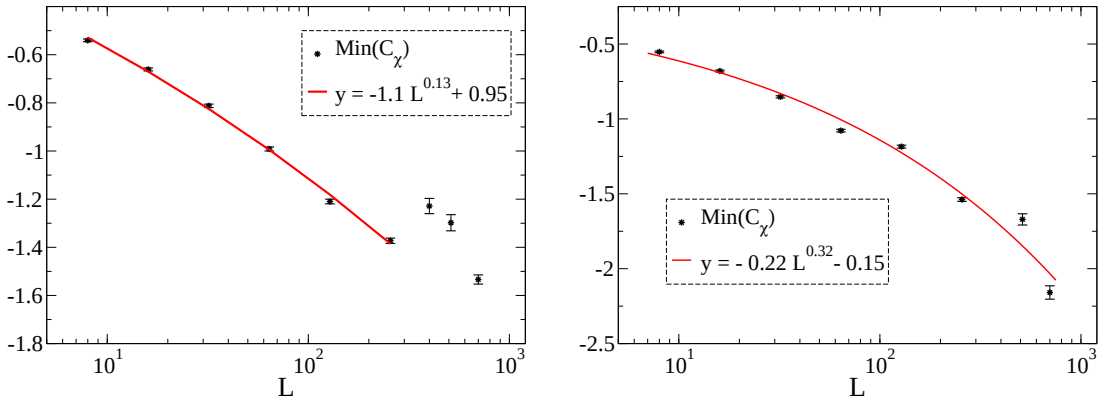

Figure 8.1: *Minimum of C_χ as a function of the lattice size.*

Left-hand side: *Free case.*

Right-hand side: *Coupled case at $g = 0.1$.*

error is estimated much higher than the errorbars indicate. In order to reach unmitigated data, it would be helpful to improve the statistics impetuously or to use a cluster algorithm.

The fit functions used here are given by

$$y = \alpha\, L^{\beta} + \gamma \ . \tag{8.1}$$

	$g = 0.0$		$g = 0.1$	
	$\mathrm{Min}(C_\chi)$	$\mathrm{Max}(C_\rho)$	$\mathrm{Min}(C_\chi)$	$\mathrm{Max}(C_\rho)$
α	-1.1	0.47	-0.22	0.41
β	0.13	0.47	0.32	0.20
γ	0.95	-0.28	-0.15	-0.22

Table 8.1: *Coefficients α, β and γ for the fit functions $y = \alpha\, L^{\beta} + \gamma$.*

The interpretation of the finite volume behavior is not straightforward. In the continuum the only symmetry of relevance is the continuous chiral symmetry (Eq. (2.20)). In 2 dimensions it is not expected to be broken spontaneously [31, 32, 33, 34, 35] and thus cannot drive a phase transition. The loop model,

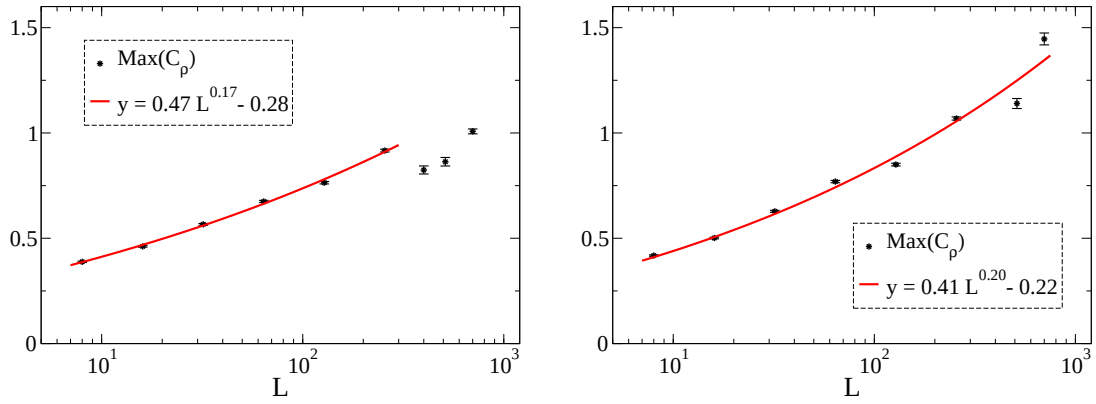

Figure 8.2: *Maximum of C_ρ as a function of the lattice size.*

Left-hand side: *Free case.*

Right-hand side: *Coupled case at $g = 0.1$.*

however, has a discrete symmetry, the interchange of red and blue loops (see Eqs. (4.15), (4.21)), which could be broken in 2 dimensions. However, the values for the exponent β are relatively small and the behavior of the peaks could also be of the form $\ln(L)$. This is a functional behavior, which would also be well compatible with the expectations from the continuum theory. Anyhow, for a sound distinction between a logarithmic divergence and a small exponent β very high statistics would be required and this question has to be left open for now.

8.2 Comparison of different boundary conditions

In Sec. 6.4, where the different initial conditions are discussed, the effect of different boundary conditions for the chiral condensate on a 32^2 lattice is shown in Fig. 6.8. Now the size dependence of this effect is analyzed numerically.

One can extract the distances between the three graphs in Fig. 6.8, for instance at $m = 0.1$, where the difference between the graphs is most obvious. The gap between the ee (even-even) and the eo (even-odd) sector $\Delta\chi^{(eo-ee)}$ (introduced in Sec. 6.4) as well as the gap between the ee and the oo (odd-odd) sector $\Delta\chi^{(oo-ee)}$

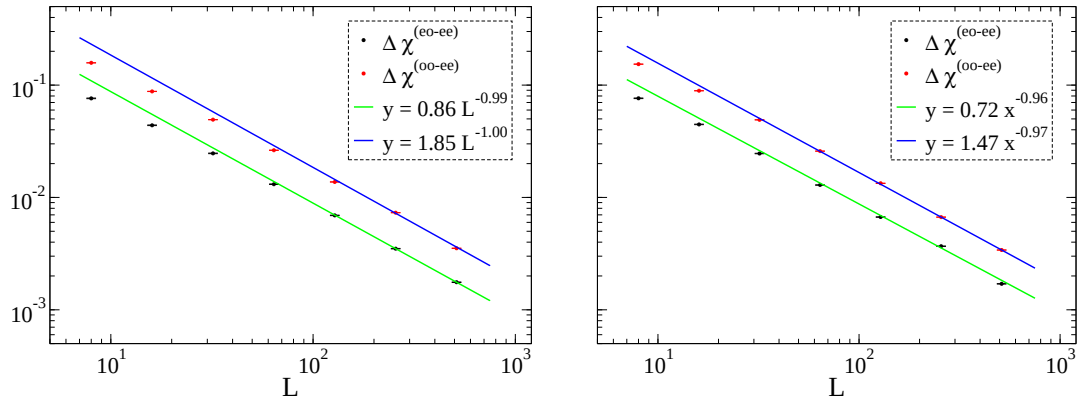

Figure 8.3: $\Delta\chi$ *as a function of the lattice size for mass parameter* $m = 0.1$.

Left-hand side: *Free case.*

Right-hand side: *Coupled case at* $g = 0.1$.

is evaluated for several lattice sizes in the free and the coupled case. Using a logarithmic scale in Fig. 8.3 brings the data sets into an approximately linear form. This is shown by the straight lines, which are fits to a straight line using only the data for the three largest lattices. The corresponding fit functions are given by

$$y = \alpha\, L^{\beta}\ , \tag{8.2}$$

with α, β being real numbers. β denotes the slopes of the straight lines on the logarithmic scale, its values are given in Tab. 8.2.

	$g = 0.0$		$g = 0.1$	
	eo - ee	oo - ee	eo - ee	oo - ee
α	0.86	1.85	0.72	1.47
β	-0.99	-1.00	-0.96	-0.97

Table 8.2: *Coefficients* α *and* β *for the fit functions* $\Delta\chi = \alpha\, L^{\beta}$.

Since the values of the slopes of all straight lines are very close to -1, one can estimate the finite size effect to be proportional to $\frac{1}{L}$. This result nicely confirms the mechanism for the finite size effect, which is discussed using mean-field arguments in Sec. 6.4 (in particular formulas (6.15)-(6.18) show that the

leading effects should scale as $\frac{1}{L}$). Also the relative factor of 2 between the eo-ee and the oo-ee finite size effect is found here. The overall amplitude is not predicted as is discussed in Sec. 6.4.

Chapter 9

Comparison with standard methods

The best verification for the fermion loop representation is the free case because analytic results are available for a comparison. Since the parameters f_1 and f_2 are smooth functions of both, g and m, the free case is not particularly special in the fermion loop representation. That means, if the free case matches with the analytic results, then the coupled case is expected to be correct, too. Of course, in spite of this fact, it is indispensable to check also the coupled case.

Using the standard approach it is rather awkward to compute the interaction susceptibility. This is the reason why only the chiral condensate, the mass susceptibility and the interaction density are compared to analytic results (free case) and to results from the standard formulation for the coupled case in this chapter. Markus Limmer (see [36]) has provided the data for the observables computed with the standard approach.

9.1 The standard approach

In the standard approach one takes the formulation of the partition function in Eq. (3.25), where the fermion fields are integrated out. Hence, the expectation values (Eq. (2.1)) are given by

$$\langle O \rangle_\phi = \frac{\int \prod_{\mathbf{n}\in\Lambda} \mathrm{d}\phi(\mathbf{n}) \det[M^{[\phi]}]\, e^{-\frac{1}{2g}\sum_{\mathbf{n}} \phi^2(\mathbf{n})} O(M^{[\phi]}, \phi)}{\int \prod_{\mathbf{n}\in\Lambda} \mathrm{d}\phi(\mathbf{n}) \det[M^{[\phi]}]\, e^{-\frac{1}{2g}\sum_{\mathbf{n}} \phi^2(\mathbf{n})}} \,. \tag{9.1}$$

Applying a MC simulation one replaces the integrals by sums over the number of measurements. The configurations ϕ_i (ϕ_i denotes $|\Lambda|$ values $\phi(\mathbf{n})$) have a Gaussian distribution. They are generated with the Box-Muller [37] algorithm. Then, observables can be computed according to

$$\langle O \rangle_\phi = \frac{\sum_{i=1}^{N} \det(M^{[\phi]})_i \, O(M^{[\phi]}, \phi)_i}{\sum_{i=1}^{N} \det(M^{[\phi]})_i} \ , \tag{9.2}$$

where the configurations are re-weighted with the determinant. The determinant can be computed using LAPACK routines (see [36, 38]).

9.2 Chiral condensate and mass susceptibility

To compute the chiral condensate χ in the standard approach, one uses Wick's theorem (introduced in Sec. 3.2.2) to rewrite the chiral condensate from its formulation in Eq. (7.2):

$$\chi = \frac{1}{|\Lambda|} \sum_{\mathbf{n}} \langle \bar{\psi}(\mathbf{n}) \psi(\mathbf{n}) \rangle = -\frac{1}{|\Lambda|} \left\langle \sum_{\mathbf{n}} M^{-1}(\mathbf{n}, \mathbf{n})_{\alpha\alpha} \right\rangle_\phi \ . \tag{9.3}$$

The Dirac indices α (and in the next formula β) are summed over. Analogously, the mass susceptibility can be written as

$$\begin{aligned} C_\chi &= \frac{1}{|\Lambda|} \frac{\partial}{\partial m} \sum_{\mathbf{n}} \langle \bar{\psi}(\mathbf{n}) \psi(\mathbf{n}) \rangle \\ &= \frac{1}{|\Lambda|} \left\langle \sum_{\mathbf{n}} M^{-1}(\mathbf{n}, \mathbf{n})_{\alpha\alpha} \right\rangle_\phi^2 - \frac{1}{|\Lambda|} \left\langle \left(\sum_{\mathbf{n}} M^{-1}(\mathbf{n}, \mathbf{n})_{\alpha\alpha} \right)^2 \right\rangle_\phi \\ &\quad + \frac{1}{|\Lambda|} \left\langle \sum_{\mathbf{n},\mathbf{m}} M^{-1}(\mathbf{n}, \mathbf{m})_{\alpha\beta} \ M^{-1}(\mathbf{m}, \mathbf{n})_{\beta\alpha} \right\rangle_\phi \ . \end{aligned} \tag{9.4}$$

A special case is the free case. The scalar field ϕ can be set equal to zero. This means that the Dirac matrix is a simple differential operator and its inverse can easily be obtained from Fourier transformation (see App. A). No summation over configurations ϕ_i is necessary.

Figs. 9.1 and 9.2 show results for the chiral condensate and the mass susceptibility in the free case in both representations for some lattice sizes.

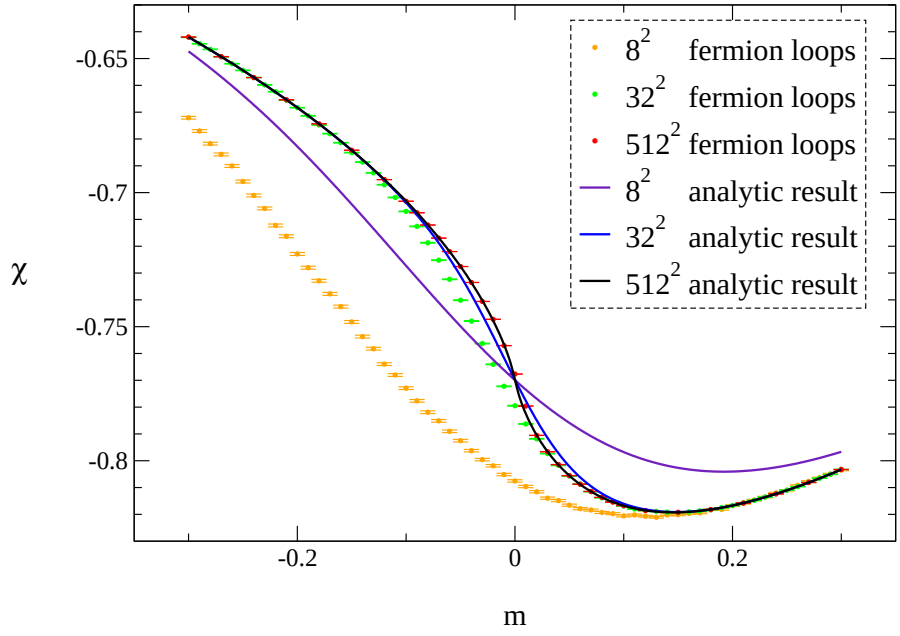

Figure 9.1: *Comparison of χ for the two different methods in the free case.*

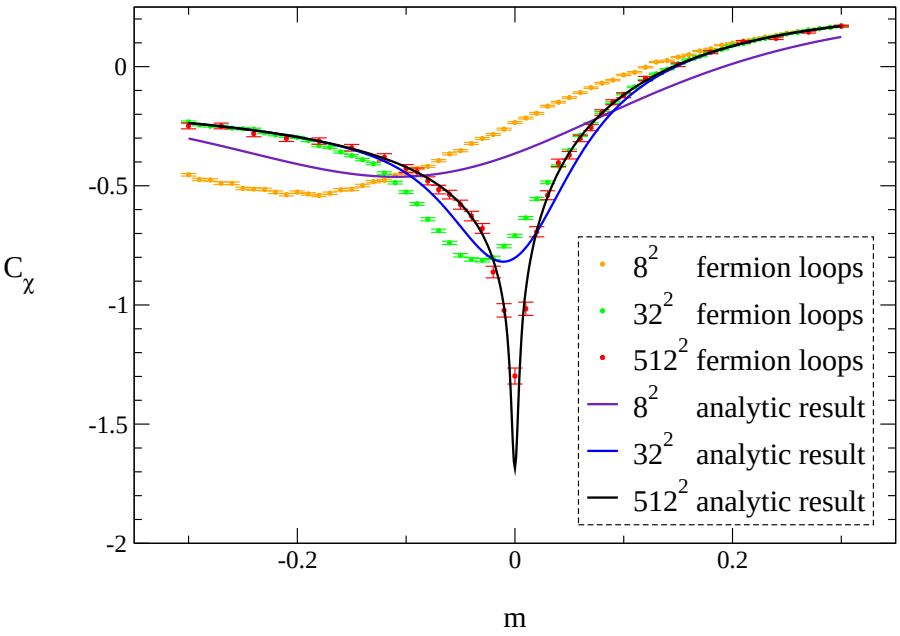

Figure 9.2: *Comparison of C_χ for the two different methods in the free case.*

Obviously, there is a clear difference between the data sets for the chiral condensate produced on a 8^2 lattice and it is still recognizable for the 32^2 lattice. The data sets from the 512^2 lattice calculations lie exactly on top of each other within errorbars. Concerning the mass susceptibility the conclusions are the same, but the correspondence at $m = 0.0$ is not as perfect as for the condensate. This is, however, not a surprise, since second derivatives of the free energy, such as the susceptibility, are much harder to evaluate numerically.

Where does this discrepancy for smaller lattice sizes come from? One reason are different boundary conditions, of course. Three choices are possible on a square lattice in the standard approach (concerning space and time direction):

- periodic - periodic boundary conditions.
- periodic - anti-periodic boundary conditions.
- anti-periodic - anti-periodic boundary conditions.

The results for the chiral condensate of the 3 different boundary conditions are presented in Fig. 9.3 for the free case. In the fermion loop representation one has the three sectors for the loops discussed in Sec. 6.4. The different boundary conditions, or sectors respectively, of the two representations do not correspond to each other one to one. A possible mapping between the different types of boundary effects in the two representations was not found so far, but also cannot be excluded.

The decisive point is that boundary conditions become less important with enlarging the system as the boundaries are of order L, whereas the 2-dimensional system increases according to L^2 (there are no massless excitations in 2 dimensions). Finite size effects behave like $\frac{1}{L}$. For the free case this fact is confirmed in Fig. 9.4, where the gaps between analytic results (periodic - anti-periodic boundary conditions) and the 3 sectors considered in the loop approach are depicted. Only data points up to a 128^2 lattice are used for the fit functions. Beyond this size it is assumed that autocorrelation interferes distinctly in the loop approach. All the fit functions reproduce the $\frac{1}{L}$ behavior and hence, one rightly concludes that both approaches match in the thermodynamic limit.

The coupled case is presented in Figs. 9.5 and 9.6. It is not possible to get data sets for lattice sizes larger than 32^2 in the standard approach because of the high demand for computer time and memory of the standard approach. Therefore, only results for calculations on a 16^2 and a 32^2 lattice can be provided.

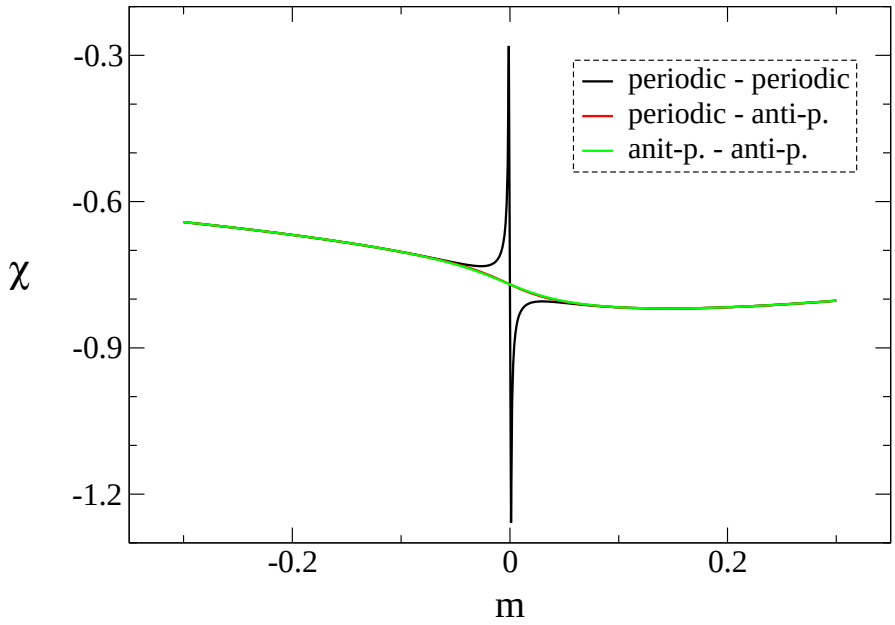

Figure 9.3: *χ as a function of the mass parameter m in the free case ($g = 0.0$) for different boundary conditions in the standard approach. The data for the anti-periodic - anti-periodic case lie exactly on top of the periodic - anti-periodic data.*

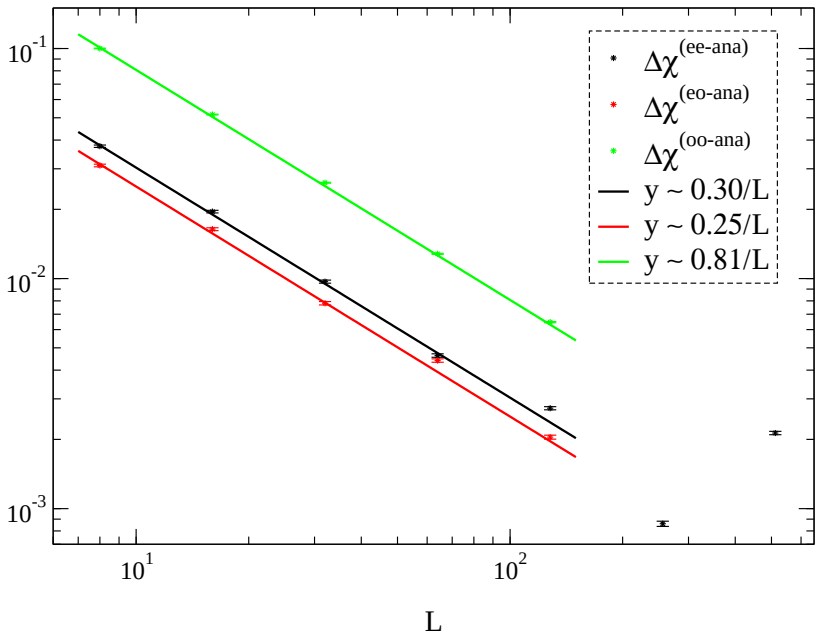

Figure 9.4: *$\frac{1}{L}$ behavior of different boundary conditions ($g = 0.0$, $m = 0.0$). The gaps between analytic results and the 3 sectors of the loop approach are depicted. y is a fit function for each data set. The 2 measure points of the large lattices corresponding to the ee sector are omitted.*

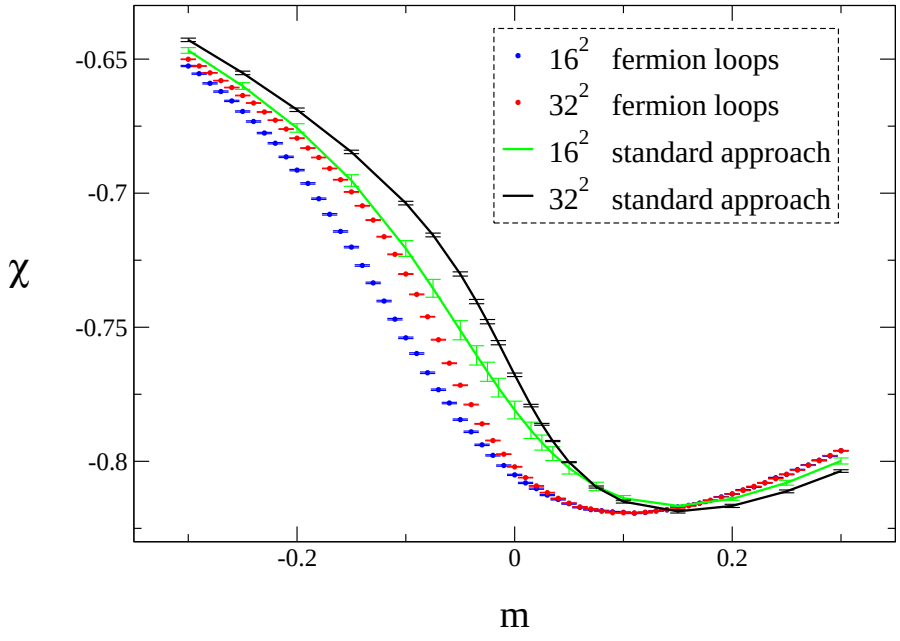

Figure 9.5: *Comparison of χ for the two different methods in the coupled case ($g = 0.1$).*

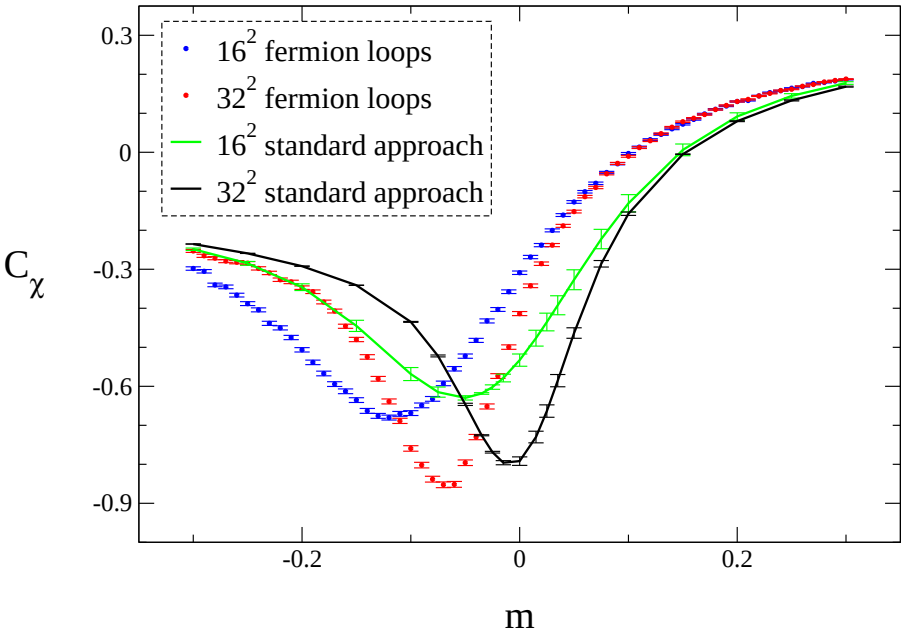

Figure 9.6: *Comparison of C_χ for the two different methods in the coupled case ($g = 0.1$).*

Comparing the free and the coupled case, e.g., on a 32^2 lattice, one recognizes that the data sets match much better in the free case. The mechanism underlying this fact is clear: Both weight factors f_1 and f_2 decrease with increasing coupling g. This implies that for increasing g the occupation of sites goes down. The occupied lines that are enforced in the eo and oo sectors thus become more important and the finite size effects more prominent. However, although it seems that the data sets might not approximate each other so quickly when enlarging L, there are some further hints that they do: Both representations show that the data sets develop similarly. The curves of the chiral condensate become a bit steeper and the change in the sign of the curvature shifts in positive direction. Regarding the mass susceptibilities, one can see that the "peak" becomes more pronounced and its modulus increases with enlarging the lattice. In spite of not being able to compare standard and loop approach on large lattices, due to the exploding numerical cost for a standard simulation, there is no doubt that the methods agree in the thermodynamic limit.

9.3 Interaction density

Again, the standard approach uses Wick's theorem (Sec. 3.2.2) to express observables in terms of inverse Dirac matrices. The interaction density reads

$$\begin{aligned}\rho &= \frac{1}{|\Lambda|}\sum_{\mathbf{n}}\left\langle\left(\bar{\psi}(\mathbf{n})\psi(\mathbf{n})\right)^2\right\rangle \\ &= \frac{1}{|\Lambda|}\left\langle\sum_{\mathbf{n}} M^{-1}(\mathbf{n},\mathbf{n})_{\alpha\alpha}M^{-1}(\mathbf{n},\mathbf{n})_{\beta\beta}\right\rangle_{\phi} \\ &\quad - \frac{1}{|\Lambda|}\left\langle\sum_{\mathbf{n}} M^{-1}(\mathbf{n},\mathbf{n})_{\alpha\beta}M^{-1}(\mathbf{n},\mathbf{n})_{\beta\alpha}\right\rangle_{\phi} . \end{aligned} \tag{9.5}$$

The two plots of the interaction density for the free and the coupled case (Figs. 9.7 and 9.8) emphasize once more that the data sets are closer to each other for the free case. The reason for this behavior are different boundary conditions being more decisive in the coupled case (see previous section). Furthermore, it is obvious that in the thermodynamic limit the results from the two methods approximate each other.

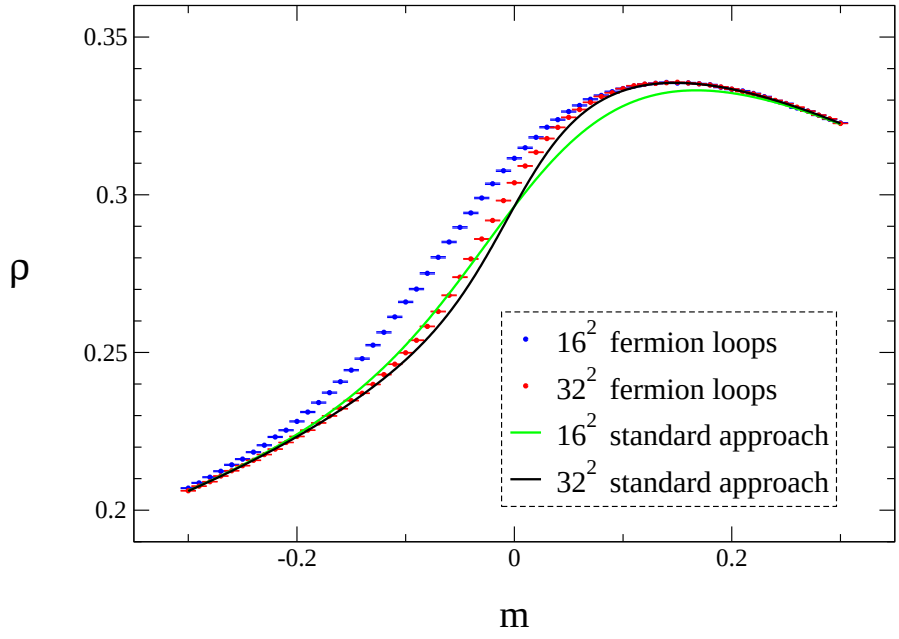

Figure 9.7: *Comparison of ρ for the two different methods in the free case.*

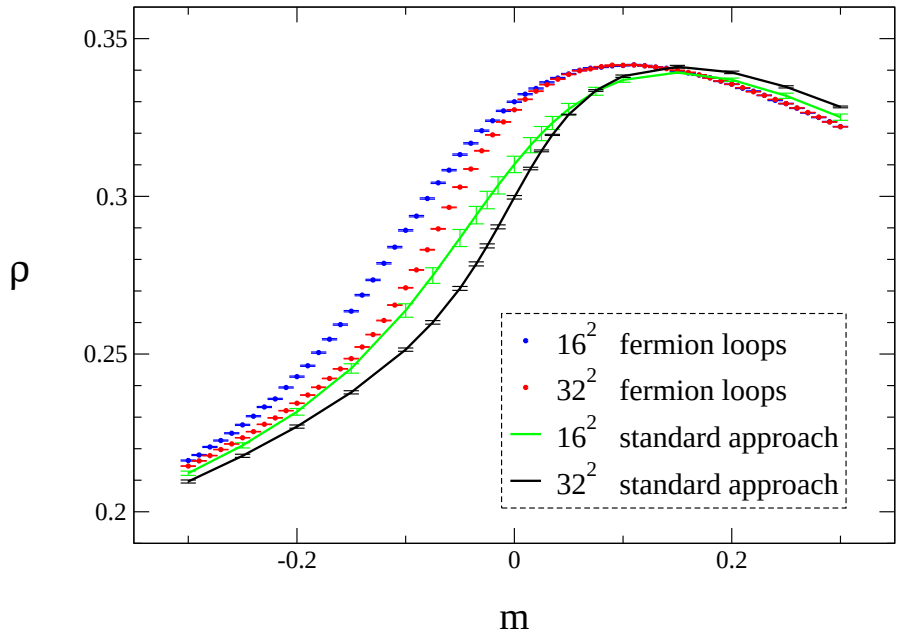

Figure 9.8: *Comparison of ρ for the two different methods in the coupled case ($g = 0.1$).*

Chapter 10

Scalar 2-point functions

In this chapter scalar 2-point functions are discussed. The expression for their calculation in the fermion loop representation is derived and the results are presented. A comparison with the standard approach is complied in the second part.

10.1 2-point functions in the loop approach

As introduced in Secs. 2.1 and 2.2, 2-point functions are computed as

$$\langle O_2(t)\, O_1(0)\rangle = \frac{1}{Z}\int \mathrm{D}[\psi,\bar{\psi},\phi]\; e^{-S[\psi,\bar{\psi},\phi]}\; O_2(t)\, O_1(0)\;. \tag{10.1}$$

A possible choice for $O_2(t)$ and $O_1(0)$ are $\bar{\psi}(\mathbf{n})\psi(\mathbf{n})$ and $\bar{\psi}(\mathbf{m})\psi(\mathbf{m})$. To be able to extract these observables from the path integral formalism, one additionally inserts an auxiliary scalar field θ into the Dirac matrix:

$$M^{[\phi]}(\mathbf{n},\mathbf{m}) = [2+m+\phi(\mathbf{n})-\theta(\mathbf{n})]\,\delta_{\mathbf{n},\mathbf{m}} - \sum_{\mu=\pm1}^{\pm2}\Gamma_\mu\delta_{\mathbf{n}+\hat{\mu},\mathbf{m}}\;. \tag{10.2}$$

This makes the partition function θ-dependent and turns it into a generating functional. Computing the second derivative of the free energy with respect to the $\theta(\mathbf{n})$ and setting $\theta = 0$, one obtains

$$\left.\frac{\partial^2 \ln Z_{GN}}{\partial\theta(\mathbf{m})\partial\theta(\mathbf{n})}\right|_{\theta=0} = \left\langle\bar{\psi}(\mathbf{n})\psi(\mathbf{n})\bar{\psi}(\mathbf{m})\psi(\mathbf{m})\right\rangle - \left\langle\bar{\psi}(\mathbf{n})\psi(\mathbf{n})\right\rangle\left\langle\bar{\psi}(\mathbf{m})\psi(\mathbf{m})\right\rangle\;. \tag{10.3}$$

Fourier transformation leads to the final form of the correlator:

$$G(m_2,n_2) = \frac{1}{{L_1}^2}\sum_{n_1,m_1=1}^{L_1}\Big[\,\big\langle\,\bar\psi(n_1,n_2)\psi(n_1,n_2)\bar\psi(m_1,m_2)\psi(m_1,m_2)\,\big\rangle - \big\langle\bar\psi(n_1,n_2)\psi(n_1,n_2)\big\rangle\,\big\langle\bar\psi(m_1,m_2)\psi(m_1,m_2)\big\rangle\,\Big]\ . \quad (10.4)$$

Using the fermion loop representation (Eq. (4.15)) the derivative of the free energy with respect to θ at $\theta = 0$ reads

$$\left.\frac{\partial \ln Z_{GN}}{\partial\theta(\mathbf{m})}\right|_{\theta=0} = \frac{1}{Z_{GN}}\sum_{C_a,C_b\in\mathcal{C}}\left(\frac{1}{\sqrt{2}}\right)^{c(C_a)+c(C_b)}\prod_{\mathbf{n}\neq\mathbf{m}}\int\frac{\mathrm{d}\phi(\mathbf{n})}{\sqrt{2\pi g}}e^{-\frac{1}{2g}\phi^2(\mathbf{n})}\,[h(\mathbf{n})]^{(2-J(\mathbf{n}))} \times\begin{cases}0 & J(\mathbf{m})=2\\ -1 & J(\mathbf{m})=1\\ -2(2+m+\phi(\mathbf{m})) & J(\mathbf{m})=0\end{cases}\ . \quad (10.5)$$

In terms of expectation values it can be written as

$$\left.\frac{\partial \ln Z_{GN}}{\partial\theta(\mathbf{m})}\right|_{\theta=0} = -\frac{f_2}{f_1}\left\langle\delta_{J(\mathbf{m}),1}\right\rangle - 2f_1\left\langle\delta_{J(\mathbf{m}),0}\right\rangle\ . \quad (10.6)$$

Analogously, the second derivative for $\mathbf{n}\neq\mathbf{m}$ can be expressed as

$$\left.\frac{\partial^2 \ln Z_{GN}}{\partial\theta(\mathbf{m})\partial\theta(\mathbf{n})}\right|_{\theta=0} = \left\langle\left[-\frac{f_2}{f_1}\delta_{J(\mathbf{n}),1}-2f_1\delta_{J(\mathbf{n}),0}\right]\left[-\frac{f_2}{f_1}\delta_{J(\mathbf{m}),1}-2f_1\delta_{J(\mathbf{m}),0}\right]\right\rangle - \left\langle-\frac{f_2}{f_1}\delta_{J(\mathbf{n}),1}-2f_1\delta_{J(\mathbf{n}),0}\right\rangle\left\langle-\frac{f_2}{f_1}\delta_{J(\mathbf{m}),1}-2f_1\delta_{J(\mathbf{m}),0}\right\rangle. \quad (10.7)$$

Due to translation invariance the expectation values of the second line in Eq. (10.7) are independent of $\mathbf{n}$ and $\mathbf{m}$. Therefore, they can be rewritten as the chiral condensate (see Eq. (7.3))

$$\left\langle-\frac{f_2}{f_1}\delta_{J(\mathbf{n}),1}-2f_1\delta_{J(\mathbf{n}),0}\right\rangle = -\frac{1}{|\Lambda|}\left[\frac{f_2}{f_1}<n_1>+2f_1<n_0>\right]=\chi\ . \quad (10.8)$$

Finally, the simplified expression is given by

$$\left.\frac{\partial^2 \ln Z_{GN}}{\partial\theta(\mathbf{m})\partial\theta(\mathbf{n})}\right|_{\theta=0} = \left(\frac{f_2}{f_1}\right)^2\left\langle\delta_{J(\mathbf{n}),1}\delta_{J(\mathbf{m}),1}\right\rangle + 4\,f_2\left\langle\delta_{J(\mathbf{n}),1}\delta_{J(\mathbf{m}),0}\right\rangle + 4\,{f_1}^2\left\langle\delta_{J(\mathbf{n}),0}\delta_{J(\mathbf{m}),0}\right\rangle-\chi^2\ . \quad (10.9)$$

Before applying the Fourier transformation to zero momentum, it is helpful to define the number of empty and singly occupied sites in timeslice n_2:

$$N_0(n_2) = \sum_{n_1} \delta_{J(n_1,n_2),0} \ , \qquad N_1(n_2) = \sum_{n_1} \delta_{J(n_1,n_2),1} \ . \tag{10.10}$$

One obtains

$$\begin{aligned} G(m_2,n_2) &= \frac{1}{{L_1}^2}\Bigg[\left(\frac{f_2}{f_1}\right)^2 \langle N_1(n_2)N_1(m_2)\rangle + 4f_2 \langle N_1(n_2)N_0(m_2)\rangle \\ &\qquad + 4f_1^2 \langle N_0(n_2)N_0(m_2)\rangle \Bigg] - \chi^2 \ . \end{aligned} \tag{10.11}$$

Building the sliding average is an important tool for improving the statistics. Here, n_2 is replaced by t and accordingly m_2 is written as $t+\tau$:

$$\begin{aligned} G(\tau) &= \frac{1}{L_2}\sum_{t=1}^{L_2} G(t+\tau,t) \\ &= \frac{1}{{L_1}^2 L_2}\sum_{t=1}^{L_2}\Bigg[\left(\frac{f_2}{f_1}\right)^2 \langle N_1(t+\tau)N_1(t)\rangle + 4f_2 \langle N_1(t+\tau)N_0(t)\rangle \\ &\qquad + 4f_1^2 \langle N_0(t+\tau)N_0(t)\rangle \Bigg] - \chi^2 \ . \end{aligned} \tag{10.12}$$

Fig. 10.1 shows the correlator $G(\tau)$ in the free case at $m = 0.1$ for different lattice sizes, which still can be reached by standard approach. The error bars are asymmetric, since the correlators are plotted on a logarithmic scale. Fig. 10.2 shows the correlator $G(\tau)$ in the coupled case at $m = 0.1$ for different lattice sizes. The plateaus in the center of the correlator are dropping with increasing L_1 and it is expected that they reach zero in the thermodynamic limit. It is quite evident that the statistical fluctuations for the correlators, in particular for large distances, are more pronounced than for bulk observables. This is a well-known fact in the numerical investigation of spin systems.

10.2 2-point functions in compare with the standard approach

The comparison with the standard approach is given in Fig. 10.3 for the free case and in Fig. 10.4 for the coupled case.

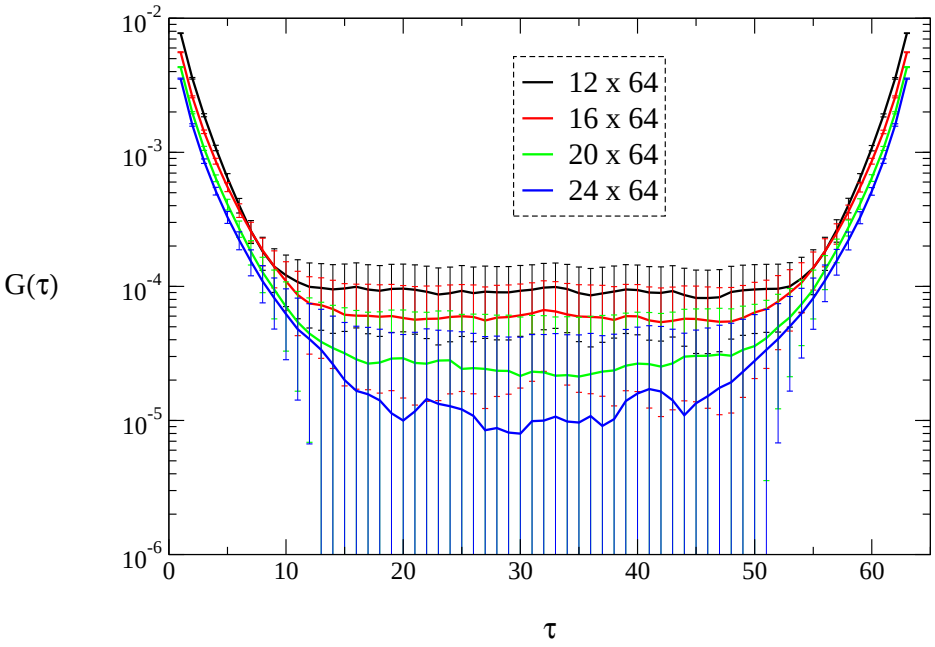

Figure 10.1: *Correlator $G(\tau)$ as a function of time τ for different lattice sizes in the free case ($g = 0.0$) at $m = 0.1$.*

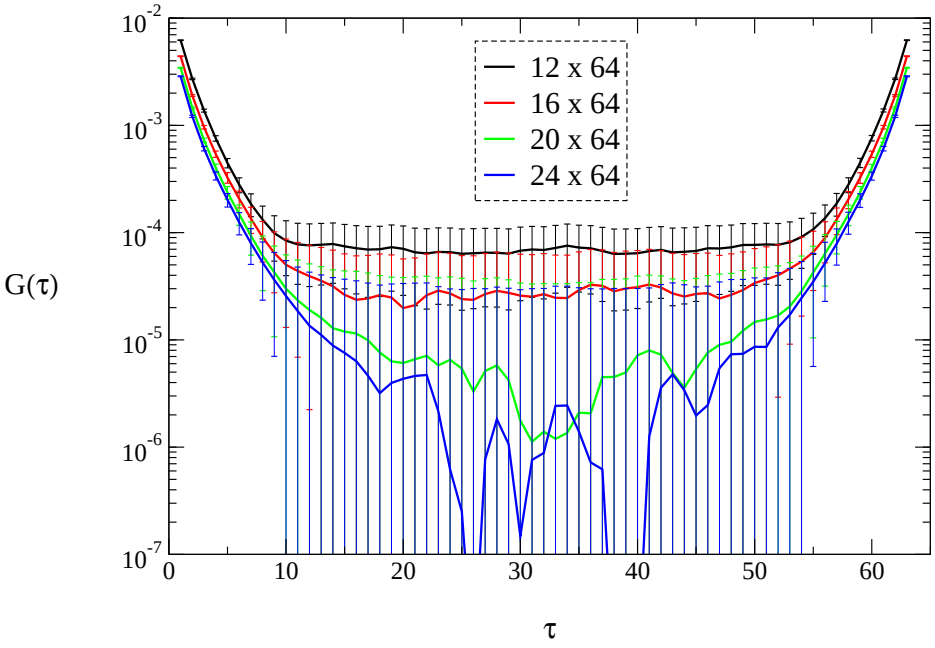

Figure 10.2: *Correlator $G(\tau)$ as a function of time τ for different lattice sizes in the coupled case ($g = 0.1$) at $m = 0.1$.*

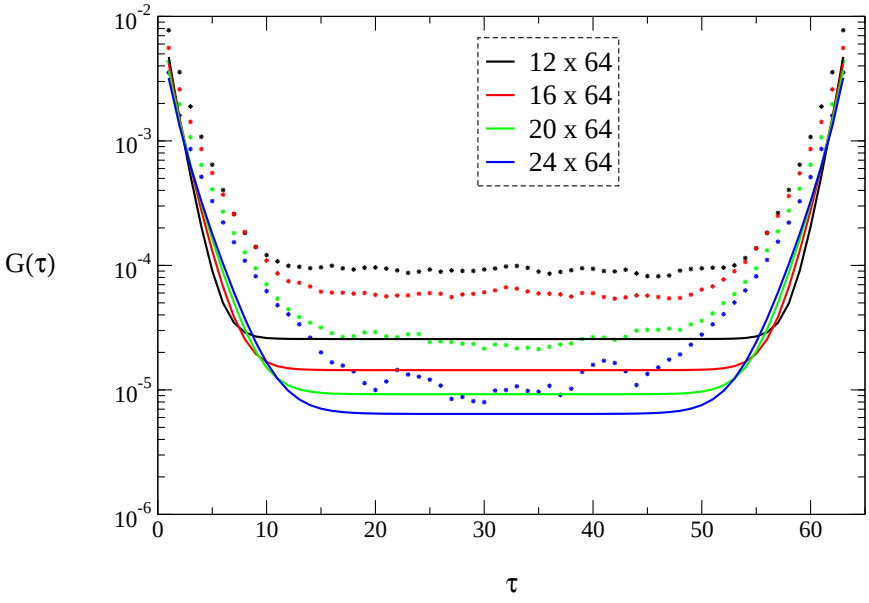

Figure 10.3: *Comparison of the correlator $G(\tau)$ for the two different methods as a function of time τ for different lattice sizes in the free case ($g = 0.0$) at $m = 0.1$. The dotted data result from the loop approach (without errorbars now) and the solid lines are analytic results.*

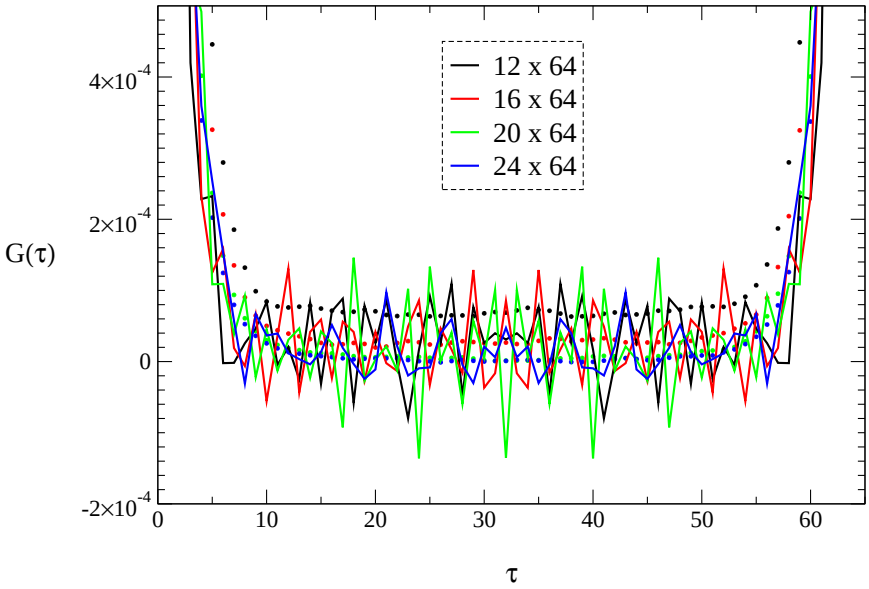

Figure 10.4: *Comparison of the correlator $G(\tau)$ for the two different methods as a function of time τ for different lattice sizes in the coupled case ($g = 0.1$) at $m = 0.1$. The dotted data result from the loop approach and the solid lines are gained from the standard approach. For a clear visualization, errorbars are omitted in both cases.*

Analytic results can be used in the free case. Obviously, both data sets (Fig. 10.3) have a similar shape and develop equivalently: For increasing the length of the lattice in space, the bottom of the plateaus drops. The remaining discrepancy is expected to originate from different boundary conditions, which cannot be neglected for lattice sizes smaller than 64^2. However, Fig. 10.1 demonstrates that the results agree within errorbars for the 24×64 lattice.

The plot for the coupled case is on a linear scale, because the large fluctuations in the standard approach lead to a few negative data points. Again, one can see that the agreement between the two representations is granted within the precision of measurements and the impact of different boundary conditions. Anyway, the data must coincide in the thermodynamic limit, since the mapping between the two representations becomes exact then.

Chapter 11

Conclusions

In general, when computing expectation values of fermionic systems in lattice QFT using a MC simulation, one has to deal with the fermion sign problem. For this reason calculations need exponentially increasing computer capacity with enlarging the volume of the system. It can be shown that there exists an alternative representation of the partition function of a 2-dimensional QFT (GN model), the fermion loop representation, which overcomes the fermion sign problem.

In this thesis an algorithm for the fermion loop representation is developed. It verifies that the mapping between the two partition functions is correct and serves as the basis to compare the advantages and disadvantages between the two approaches.

11.1 Standard approach versus loop approach

The greatest advantage of the standard approach is that it is relatively simple and general. This means that there is a lot of experience in possible implementations and many standard tools for computations exist. For example, the Box-Muller algorithm, which incurs the Gaussian distribution of the scalar fields ϕ, can easily be taken over from [37]. LAPACK routines (see [38]) handle the inversion of the Dirac matrix and compute its determinant. This is not the case in the fermion loop representation. The algorithm for the loops has to be developed step by step and tested carefully. One has to verify that it avoids self-intersections of loops that all loops are closed and one has to prove its ergodicity. It is also important

to find an optimal implementation of the algorithm, so that it runs as fast as possible and that the code remains transparent.

In the standard approach no specific representation for the partition function needs to be considered and all steps can be used for a large class of models in the same way. By contrast, in the loop approach, finding a mapping to other variables can be quite demanding and the result is specific for only the model under consideration. The fermion loop representation, as it is used in this thesis, only works for the GN model (and equivalent models) in 2 dimensions so far.

Moreover, in the fermion loop representation, one also has to find expressions for the observables in terms of loops. Troubles appear for instance with vector 2-point functions [39, 40], because probably these observables cannot be expressed in terms of non-oriented loops only (see also in the outlook, Sec. 11.2). Scalar 2-point functions can be computed, since they have the form $\langle\bar{\psi}\mathbb{1}\psi\ \bar{\psi}\mathbb{1}\psi\rangle$, while 2-point functions $\langle\bar{\psi}\gamma_\mu\psi\ \bar{\psi}\gamma_\nu\psi\rangle$ for vectors have an orientation according to the indices μ, ν. The situation is simpler for expectation values in the standard approach, which always can be calculated directly using Wick's theorem. The resulting formulas are functions of the inverse Dirac matrix and can be implemented in the computer program without reformulation.

Although there exist several disadvantages for the fermion loop representation, it has also a lot of merits. Outstanding are the drastically reduced computer requirements of the programs. Compared to the standard approach two orders of magnitude are gained. Therefore, the statistics and system sizes can be highly improved. Furthermore, the loop representation needs considerably less memory for its implementation. Calculations for fixed parameter values allow to include more than 10^6 lattice points without any problem, need only about one week of run-time on the available pc cluster and still have excellent statistics (compare Chap. 7). Enlarging the system is a decisive point, because finite size effects become less important and one approximates the thermodynamic limit much better. By contrast, the standard approach is limited to lattice sizes of 2500 lattice points (using a typical pc cluster).

> Summarizing these various aspects, it is fair to say that the fermion loop representation, as it is developed so far, needs more conceptual work compared to the standard approach. This is, however, rewarded by an increase of the efficiency by two orders of magnitude, which leads to considerably improved physical results.

11.2 Outlook

The fermion loop representation definitely can be a great advantage and its further development will be useful. Several issues should be considered:

- One of the primary aims is, of course, to be able to compute some more advanced observables, in particular vector n-point functions. The difficulty here is that each observable has to be expressed in terms of the loop representation. Since vectors are oriented objects, it might be necessary to generalize the representation to oriented loops.

- The algorithm developed in this thesis is constructed for the one flavor model. The loop representation exists for arbitrary numbers of flavors and it would be challenging to develop and test the corresponding algorithms. This is really interesting, since for more than one flavor the chiral symmetry is a discrete symmetry, which can be broken spontaneously also in 2 dimensions.

- Of particular value is the generalization of the loop approach to higher dimensions. One could imagine [41] that the loops might be replaced by closed surfaces, but up to now, no such mapping exists for a physically interesting model.

Appendix A

The doubling problem

Naively, the discretized Dirac matrix of the GN-model on the lattice would be written as

$$M^{[\phi]}(\mathbf{n},\mathbf{m}) = [m+\phi(\mathbf{n})]\,\delta_{\mathbf{n},\mathbf{m}} - \sum_{\mu=1}^{2}\gamma_\mu \frac{\delta_{\mathbf{n}+\hat{\mu},m} - \delta_{\mathbf{n}-\hat{\mu},\mathbf{m}}}{2a} \ , \tag{A.1}$$

where a is the lattice spacing. The quark propagator which governs the behavior of n-point functions is the inverse of the Dirac matrix $M^{[\phi]}(\mathbf{n},\mathbf{m})^{-1}$. One obtains the free case, when ϕ is set equal to zero. Here, $M^{[0]}(\mathbf{n},\mathbf{m})^{-1}$ can be computed with Fourier transformation

$$\mathrm{FT}[M^{[0]}(\mathbf{n},\mathbf{m})] = a^4 \frac{1}{|\Lambda|}\sum_{\mathbf{n},\mathbf{m}} e^{-\mathrm{i}\mathbf{p}\cdot\mathbf{n}\,a} M^{[0]}(\mathbf{n},\mathbf{m})\, e^{\mathrm{i}\mathbf{q}\cdot\mathbf{m}\,a} \ . \tag{A.2}$$

$\mathbf{p}$ and $\mathbf{q}$ are vectors of the lattice in momentum space, given by

$$\tilde{\Lambda} = \left\{ \mathbf{p}=(p_1,p_2) \ \middle| \ p_\mu = \frac{2\pi}{aL_\mu} n_\mu \ \ ; \ n_\mu = 1,\ldots,L_\mu \right\} \ . \tag{A.3}$$

One finds

$$\mathrm{FT}[M^{[0]}(\mathbf{n},\mathbf{m})] = a^4\, \tilde{M}(\mathbf{p})\,\delta(\mathbf{p}-\mathbf{q}) \ , \tag{A.4}$$

with

$$\tilde{M}(\mathbf{p}) = m\mathbb{1} + \frac{\mathrm{i}}{a}\sum_{\mu=1}^{2}\gamma_\mu \sin(p_\mu a) \ , \tag{A.5}$$

where obviously all elements non-diagonal in $\mathbf{p}$ vanish. Inverting the 2×2 matrix $\tilde{M}(\mathbf{p})$, one finds [3]

$$\tilde{M}(\mathbf{p})^{-1} = \frac{m\mathbb{1} - \mathrm{i}a^{-1}\sum_\mu \gamma_\mu \sin(p_\mu a)}{m^2 + a^{-2}\sum_\mu \sin(p_\mu a)^2} \ . \tag{A.6}$$

Although the correct continuum limit ($a \to 0$) is reached for fixed $\mathbf{p}$, there remain additional poles for $p = (0, \frac{\pi}{a}), (\frac{\pi}{a}, 0), (\frac{\pi}{a}, \frac{\pi}{a})$ at $m = 0$ due to the sine functions which appear on the lattice. The physical pole is $p = (0, 0)$.

The other poles, so-called doublers, can be removed by augmenting the Dirac operator in momentum space with the so-called *Wilson term*

$$\tilde{M}(\mathbf{p}) = m\mathbb{1} + \frac{\mathrm{i}}{a}\sum_{\mu=1}^{2}\gamma_\mu \sin(p_\mu a) + \mathbb{1}\frac{1}{a}\sum_{\mu=1}^{2}(1 - \cos(p_\mu a)) \ . \tag{A.7}$$

Now, the doubler poles ($p_\mu = \frac{\pi}{a}$) acquire a mass $\propto \frac{1}{a}$ which diverges in the continuum limit $a \to 0$. Thus, the doublers decouple then.
The Dirac operator in position space can be found by inverse Fourier transformation. It reads (the scalar field ϕ is now coupled again)

$$M^{[\phi]}(\mathbf{n}, \mathbf{m}) = \left(m + \frac{2}{a} + \phi(\mathbf{n})\right)\delta_{\mathbf{n},\mathbf{m}} - \frac{1}{2a}\sum_{\mu=\pm1}^{\pm2}(\mathbb{1} - \gamma_\mu)\,\delta_{\mathbf{n}+\hat{\mu},\mathbf{m}} \ , \tag{A.8}$$

with $\gamma_{-\mu} = -\gamma_\mu$. For small a it has the behavior

$$m + \phi(\mathbf{n}) + \gamma_\mu\partial_\mu + \frac{a}{2}\Delta + O(a^2) \ . \tag{A.9}$$

The Wilson term is the term proportional to the Laplace operator. The proportionality constant is the lattice spacing a. Thus, in the continuum limit ($a \to 0$) the Wilson term becomes irrelevant.

Appendix B

Computing the norm of the hopping matrix $R(\mathbf{n},\mathbf{m})$

For the hopping expansion (needed in Chap. 4) to converge, one has to require the condition

$$\|R(\mathbf{n},\mathbf{m})\| = \left\| \sum_{\mu=\pm 1}^{\pm 2} \Gamma_\mu \, \frac{1}{h(\mathbf{n})} \, \delta_{\mathbf{n}+\hat{\mu},\mathbf{m}} \right\| \leq 1 \; . \tag{B.1}$$

As defined in Sec. 4.1, $h(\mathbf{n})$ is given by

$$h(\mathbf{n}) = 2 + m + \phi(\mathbf{n}) \; . \tag{B.2}$$

Assumed that $h(\mathbf{n})$ fulfills the condition

$$\left\| \frac{1}{h(\mathbf{n})} \right\| < \frac{1}{2} \qquad \forall \; \mathbf{n} \; , \tag{B.3}$$

one has to show that the remaining part $H = \sum \Gamma_\mu \delta_{\mathbf{n}+\hat{\mu},\mathbf{m}}$ is bounded by the value 2:

$$\|R(\mathbf{n},\mathbf{m})\| < \frac{1}{2}\|H(\mathbf{n},\mathbf{m})\| \leq 1 \; . \tag{B.4}$$

H can be decomposed into

$$H(\mathbf{n},\mathbf{m}) = H_1(\mathbf{n},\mathbf{m}) + H_2(\mathbf{n},\mathbf{m}) \; , \tag{B.5}$$

where $H_\mu(\mathbf{n},\mathbf{m}), (\mu = 1,2)$, is given by

$$H_\mu(\mathbf{n},\mathbf{m}) = \frac{1}{2}(1-\gamma_\mu)\delta_{\mathbf{n}+\hat{\mu},\mathbf{m}} + \frac{1}{2}(1+\gamma_\mu)\delta_{\mathbf{n}-\hat{\mu},\mathbf{m}} \; . \tag{B.6}$$

Applying the triangle inequality one obtains

$$\|H\| = \|H_1 + H_2\| \leq \|H_1\| + \|H_2\| \ . \tag{B.7}$$

So, each H_1 and H_2 must not be greater than 1. Using the definition of the norm,

$$\|H_\mu\| \equiv \max_{\mathbf{v}, \|\mathbf{v}\|=1} \|H_\mu \mathbf{v}\| \ , \tag{B.8}$$

one finds

$$\|H_\mu \mathbf{v}\| = \sqrt{(H_\mu \mathbf{v})^\dagger H_\mu \mathbf{v}} = \sqrt{\mathbf{v}^\dagger H_\mu^\dagger H_\mu \mathbf{v}} = \sqrt{\mathbf{v}^\dagger \mathbf{v}} = \|\mathbf{v}\| = 1 \ , \tag{B.9}$$

where in the last step $H_\mu^\dagger H_\mu = \mathbb{1}$ was used. This can easily be seen to hold with the equations

$$\begin{aligned} (1 + \gamma_\mu)(1 - \gamma_\mu) &= 0 \ , \\ (1 \pm \gamma_\mu)^2 &= 2(1 \pm \gamma_\mu) \ , \\ H_\mu^\dagger(\mathbf{n}, \mathbf{m}) &= \tfrac{1}{2}(1 + \gamma_\mu)\delta_{\mathbf{n}-\hat{\mu}, \mathbf{m}} + \tfrac{1}{2}(1 - \gamma_\mu)\delta_{\mathbf{n}+\hat{\mu}, \mathbf{m}} \ . \end{aligned} \tag{B.10}$$

References

[1] S. Chandrasekharan and U.-J. Wiese, *Meron-cluster solution of a fermion sign problem*, *Phys. Rev. Lett.* **83**, 3116–3119 (1999).

[2] D. J. Gross and A. Neveu, *Dynamical Symmetry Breaking in Asymptotically Free Field Theories*, *Phys. Rev.* **D10**, 3235 (1974).

[3] C. Gattringer and C. B. Lang, *QCD on the Lattice - An Introduction for Beginners*, *unpublished notes.*

[4] C. Cohen-Tannoudji, B. Diu, and F. Laloë, *Quantum Mechanics*, *John Wiley and Sons,* New York, London, Sidney, Toronto (1977).

[5] J. E. Hirsch, *Discrete Hubbard-Stratonovich Transformation for Fermion Lattice Models*, *Phys. Rev.* **B28**, 4059–4061 (1983).

[6] J. E. Hirsch, *Erratum: Discrete Hubbard-Stratonovich Transformation for Fermion Lattice Models*, *Phys. Rev.* **B29**, 4159 (1984).

[7] Y. Nambu and G. Jona-Lasinio, *Dynamical Model of Elementary Particles based on an Analogy with Superconductivity I*, *Phys. Rev.* **122**, 345–358 (1961).

[8] Y. Nambu and G. Jona-Lasinio, *Dynamical Model of Elementary particles based on an Analogy with Superconductivity II*, *Phys. Rev.* **124**, 246–254 (1961).

[9] W. E. Thirring, *A Soluble Relativistic Field Theory*, *Annals Phys.* **3**, 91–112 (1958).

[10] I. Montvay and G. Münster, *Quantum Fields on a Lattice*, *Cambridge, UK: Univ. Pr.* 491 p. (Cambridge monographs on mathematical physics) (1994).

[11] M. Creutz, *Quarks, Gluons and Lattices*, *Cambridge, Uk: Univ. Pr.* 169 p. (Cambridge Monographs On Mathematical Physics) (1983).

[12] J. Smit, *Introduction to Quantum Fields on a Lattice: A Robust Mate*, *Cambridge Lect. Notes Phys.* **15**, 1–271 (2002).

[13] F. Wegner, *Graßmann-Variable*, Universität Heidelberg, http://www.tphys.uni-heidelberg.de/∼wegner/SS01.html (1998).

[14] G. C. Wick, *The Evaluation of the Collision Matrix*, *Phys. Rev.* **80**, 268–272 (1950).

[15] K. Scharnhorst, *The Exact Equivalence of the One-Flavour Lattice Thirring Model with Wilson Fermions to a Two-Colour Loop Model*, *Nucl. Phys.* **B503**, 479–504 (1997).

[16] C. Gattringer, *Loop Representation for 2-D Wilson Lattice Fermions in a Scalar Background Field*, *Nucl. Phys.* **B543**, 533–542 (1999).

[17] C. Gattringer, *A Formula for the Hopping Expansion of 8-Vertex Models Coupled to an External Field*, *Int. J. Mod. Phys.* **A14**, 4853 (1999).

[18] I. O. Stamatescu, *A Note on the Lattice Fermionic Determinant*, *Phys. Rev.* **D25**, 1130 (1982).

[19] C. R. Gattringer, S. Jaimungal, and G. W. Semenoff, *Loops, Surfaces and Grassmann Representation in Two- and Three-Dimensional Ising Models*, *Int. J. Mod. Phys.* **A14**, 4549–4574 (1999).

[20] C. Gattringer, *Hopping Expansion as a Tool for Handling Dual Variables in Lattice Models*, *Nucl. Phys. Proc. Suppl.* **73**, 772–774 (1999).

[21] C. Fan and F. Y. Wu, *Exactly Solved Models in Statistical Mechanics*, *Phys. Rev.* **179**, 179 (1969).

[22] C. Fan and F. Y. Wu, *General Lattice Model of Phase Transitions*, *Phys. Rev.* **B2**, 723–733 (1970).

[23] R. Baxter, *Exactly Solved Models in Statistical Mechanics*, *Academic Press,* London 1982.

[24] K. Binder and D. Heermann, *Monte Carlo Simulation in Statistical Physics: An Introduction*, *Springer,* Berlin, Germany (1989).

[25] N. Metropolis, A. W. Rosenbluth, M. N. Rosenbluth, A. H. Teller, and E. Teller, *Equation of State Calculations by Fast Computing Machines*, *J. Chem. Phys.* **21**, 1087–1092 (1953).

[26] B. A. Berg, *Introduction to Markov Chain Monte Carlo Simulations and their Statistical Analysis*, *World Scientific,* Singapore, http://www.hep.fsu.edu/∼berg (2004).

[27] L. Lyons, *A Practical Guide to Data Analysis for Physical Science Students*, *Cambridge University Press,* (1991).

[28] M. Lüscher, *A Portable High Quality Random Number Generator for Lattice Field Theory Simulations*, *Comput. Phys. Commun.* **79**, 100–110 (1994).

[29] F. James, *RANLUX: A Fortran Implementation of the High Quality Pseudorandom Number Generator of Lüscher*, *Comp. Phys. Commun.* **79**, 111–114 (1994).

[30] M. Fukugita, H. Mino, M. Okawa, and A. Ukawa, *Finite Size Test for the Finite Temperature Chiral Phase Transition in Lattice QCD*, *Phys. Rev. Lett.* **65**, 816–819 (1990).

[31] P. C. Hohenberg, *Existance of Long-Range Order in One and Two Dimensions*, *Phys. Rev.* **158**, 383–386 (1967).

[32] N. D. Mermin and H. Wagner, *Absence of Ferromagnetism or Antiferromagnetism in One- Dimensional or Two-Dimensional Isotropic Heisenberg Models*, *Phys. Rev. Lett.* **17**, 1133–1136 (1966).

[33] N. D. Mermin, *Absence of Ordering in Certain Classical Systems*, *Journ. Math. Phys.* **8**, 1061 (1967).

[34] S. R. Coleman, *Quantum Sine-Gordon Equation as the Massive Thirring Model*, *Phys. Rev.* **D11**, 2088 (1975).

[35] S. R. Coleman, *There are No Goldstone Bosons in Two-Dimensions*, *Commun. Math. Phys.* **31**, 259–264 (1973).

[36] M. Limmer, *Lattice Simulation of Gross-Neveu-type Models*, *Diploma thesis,* Universität Regensburg (2006).

[37] W. H. Press, S. A. Teukolsky, W. T. Vetterling, and B. Flannery, *Numerical Recipes in C: The Art of Scientific Computing*, *Cambridge University Press,* New York (1992).

[38] http://www.netlib.org/lapack/

[39] M. Karowski, R. Schrader, and H. J. Thun, *Monte Carlo Simulations For Quantum Field Theories Involving Fermions*, *Commun. Math. Phys.* **97**, 5 (1985).

[40] C. Gattringer, *The Lattice Schwinger Model as a Discrete Sum of Filled Wilson Loops*, *Nucl. Phys.* **B559**, 539–562 (1999).

[41] C. Gattringer and E. Bilgici - *work in progress.*

Acknowledgment

It's a great pleasure to thank those who contributed to the success of this work:

- Prof. Dr. Christof Gattringer, who provided me the interesting topic, kept an eye on every step I did, perpetually took his time for expedient discussions and managed to motivate me, whenever I got lost in doubt.
- Prof. Dr. Klaus Richter, who enabled me to pass my diploma thesis at his chair, continuously welcomed me and assisted my participations in conferences.
- Prof. Dr. Christian Lang and the whole lattice group in Graz for inspiring conversations.
- Erec Bilgici, Rafael Frigori, Martina Jörgler, Markus Limmer and Dominik Nickel for the pleasant atmosphere and the proper composition of sedulous working and fun in our office.
- My colleagues in Graz as well as in Regensburg for many interesting discussions and their efforts to help me with any problem I had. Amongst others I want to emphasize: Michael Hartung, Andreas Krassnigg, Bernd-Jochen Schaefer, Stefan Solbrig and Martin Volk.
- Markus Limmer for "being the judge" of my representation. Moreover, he accompanied me as a constant foothold not only in physical matters.
- And last but not least my parents, who were backing me all the way, supported me unconditionally and who I always could rely on.

Traunstein, November 2006

Garbage in - garbage out!

Old programmer's wisdom

Erklärung

Hiermit erkläre ich, dass ich die Diplomarbeit selbständig angefertigt und keine Hilfsmittel außer den in der Arbeit angegebenen benutzt habe.

Traunstein, den 30. November 2006

.....

(Verena Hermann)